Kidney organoids recapitulate human basement membrane assembly in health and disease

Mychel Raony Paiva Teixeira Morais1[§,1,7], Pinyuan Tian[§,1], Craig Lawless[1], Syed Murtuza-Baker[2], Louise Hopkinson[1], Steven Woods[3], Aleksandr Mironov[4], David Andrew Long[5], Daniel Gale[6], Telma Maria Tenorio Zorn[7], Susan Kimber[3], Roy Zent[8], Rachel Lennon*[1,9].

Affiliations

1.Wellcome Centre for Cell-Matrix Research, Division of Cell-Matrix Biology and Regenerative Medicine, School of Biological Sciences, Faculty of Biology Medicine and Health, The University of Manchester, Manchester Academic Health Science Centre, Manchester, M13 9PT, UK. 2. Division of Informatics, Imaging & Data Sciences, School of Biological Sciences, Faculty of Biology Medicine and Health, The University of Manchester, Manchester Academic Health Science Centre, Manchester, M13 9PT, UK. 3. Division of Cell Matrix Biology & Regenerative Medicine, School of Biological Sciences, Faculty of Biology Medicine and Health, The University of Manchester, Manchester Academic Health Science Centre, Manchester, M13 9PT, UK. 4. Electron Microscopy Core Facility, RRID:SCR_021147, Faculty of Biology, Medicine and Health, The University of Manchester, Manchester, M13 9PT, UK. 5. Developmental Biology and Cancer Programme, UCL Great Ormond Institute of Child Health, London, WC1N 1EH, UK. 6. Department of Renal Medicine, University College London, London, NW3 2PF, UK. 7. Department of Cell and Developmental Biology, Institute of Biomedical Sciences, University of São Paulo, São Paulo, SP, 05508-000, Brazil. 8. Department of Medicine, Vanderbilt University Medical Center, Nashville, TN, 37232, USA. 10. Department of Paediatric Nephrology, Royal Manchester Children's Hospital, Manchester University Hospitals NHS Foundation Trust, Manchester Academic Health Science Centre, Manchester, M13 9WL, UK.

Author list footnotes:

[§]These authors contributed equally to this work. *Lead correspondence contact: Rachel Lennon, rachel.lennon@manchester.ac.uk.

SUMMARY

Basement membranes (BMs) are complex macromolecular networks underlying all continuous layers of cells. Essential components include collagen IV and laminins, which are affected by human genetic variants leading to a range of debilitating conditions including kidney, muscle, and cerebrovascular phenotypes. We investigated the dynamics of BM assembly in human pluripotent stem cell-derived kidney organoids. We resolved their global BM composition and discovered a conserved temporal sequence in BM assembly that paralleled mammalian fetal kidneys. We identified the emergence of key BM isoforms, which were altered by a pathogenic variant in *COL4A5*. Integrating organoid, fetal and adult kidney proteomes we found dynamic regulation of BM composition through development to adulthood, and with single-cell transcriptomic analysis we mapped the cellular origins of BM components. Overall, we define the complex and dynamic nature of kidney BM assembly and provide a platform for understanding its wider relevance in human development and disease.

KEYWORDS

Extracellular matrix, basement membrane, fetal kidney, glomerular development, organoids, matrisome, collagen IV, laminin, Alport syndrome.

Impact statement

Kidney organoids are a high-fidelity system for investigating basement membrane regulation in development and disease.

INTRODUCTION

Basement membranes (BMs) surround tissues providing cells with an interface for physical and signaling interactions (Jayadev and Sherwood, 2017). They are composed of laminins, collagen IV, nidogens, heparan-sulfate proteoglycans (Kruegel and Miosge, 2010) and many minor components that combine to form biochemically distinct BMs across different tissues (Randles et al., 2017). BMs play active morphogenic roles that are critical for tissue and cell fate specification (Kyprianou et al., 2020; Li et al., 2003), and variants in BM genes are associated with a broad range of human diseases (Chew and Lennon, 2018; Gatseva et al., 2019). Despite increasing knowledge of BM composition and function there is limited understanding about BM regulation, yet this is required for new mechanistic insights into BM-associated human disease.

BMs form early in embryogenesis through binding interactions with cell surface receptors (Miner and Yurchenco, 2004) and typically an initial laminin network is required for further incorporation of collagen IV, nidogen and perlecan into nascent BMs (Jayadev et al., 2019; Matsubayashi et al., 2017) thus following an assembly hierarchy for *de novo* BM formation. BMs are also highly dynamic, remodeling during morphogenesis to form tissue-specific BMs (Bonnans et al., 2014), such as the glomerular basement membrane (GBM) in the kidney, which functions as a size selective filter. Situated between podocytes and endothelial cells in the glomerular capillary wall, the GBM is formed by the fusion of separate podocyte and endothelial BMs, and further remodeled into a mature GBM. This involves replacement of laminin $\alpha1\beta1\gamma1$ (termed laminin-111) and collagen IV $\alpha1\alpha1\alpha2$ networks by laminin-511 then -521, and collagen IV $\alpha3\alpha4\alpha5$ (Abrahamson et al., 2013; Abrahamson and St John, 1993). These transitions are important for long term GBM function and genetic variants in *COL4A3,* *COL4A4* and *COL4A5* or the laminin gene *LAMB2* cause defective GBMs and human disease (Barker et al., 1990; Zenker et al., 2004).

The study of BM assembly is challenging due to the technical difficulties in tracking large, spatiotemporally regulated components. Most understanding about vertebrate BMs comes from immunolocalization and genetic knock-out studies (Abrahamson et al., 2013) and for composition, mass spectrometry (MS)-based proteomics has enabled global analysis (Naba et al., 2016; Randles et al., 2015). Proteomics also allows time course studies, which have provided insight into matrix dynamics during development and in disease progression (Hebert et al., 2020; Lipp et al., 2021; Naba et al., 2017). However, proteomics lacks the spatial context that is captured by localization studies including fluorescent tagging of endogenous proteins. Such investigations in *Drosophila* and *C. elegans* have unraveled dynamic features of BM assembly in embryogenesis and repair (Howard et al., 2019; Keeley et al., 2020; Matsubayashi et al., 2020). The development of a system to study human BM assembly would facilitate investigation of both morphogenesis and disease.

Kidney organoids generated from pluripotent stem cells (PSCs) contain self-organised 3D structures with multiple kidney cell types and they represent an attractive system for investigating early development (Combes et al., 2019b; Takasato et al., 2015). Organoids derived from induced PSCs (iPSCs), reprogrammed from patient somatic cells have further use in personalized disease modelling and therapy screening (Czerniecki et al., 2018; Forbes et al., 2018). The nephron is the functional unit of the kidney and during differentiation, kidney organoids pattern into early nephron structures with clusters of podocytes and endothelial cells, and a complex tubular epithelial system. Furthermore organoids show transcriptomic homology to the first trimester human fetal kidney (Takasato et al., 2015) and differentiation is further advanced by *in vivo* implantation (Bantounas et al., 2018). Whilst understanding about cell types in kidney organoids has progressed significantly, there is a knowledge gap about extracellular matrix and BM assembly during differentiation.

We investigated BM assembly during kidney development using organoids and fetal kidney tissue. With proteomics we defined a complex sequence of BM assembly during organoid differentiation and demonstrated the utility of this experimental system for investigating BM remodelling in both early development and human disease. Furthermore, we compared the organoid matrix to the E19 mouse kidney and adult human kidney matrix and defined the cellular origins of BM components. Overall, we demonstrate that kidney organoids represent a high-fidelity system to study the dynamics of human BM assembly.

RESULTS

Kidney organoids form BM networks that are altered with defective *COL4A5*

To improve understanding of BM assembly and regulation, we investigated human kidney organoids. We differentiated wild-type iPSCs into intermediate mesoderm cells in 2D culture, and then 3D-kidney organoids (**Figures 1A** and **Figure 1–figure supplement 1A**). We confirmed differentiation to glomerular clusters (WT1$^+$/NPHS1$^+$/CD31$^+$) and CDH1$^+$ tubular structures in day 18 organoids (**Figure 1B**) and compared morphology to mouse and human fetal kidney tissue. Day 11 organoids had cell clusters amongst mesenchymal tissue, and at day 14, discernable nephron-like structures (**Figure 1–figure supplement 1A**). At day 18, organoids had regions resembling the nephrogenic zone at embryonic day 19 (E19) in the mouse and between 8-10 wpc in human but lacked distinct cortico-medullary differentiation (**Figures 1C** and **Figure 1–figure supplement 1A**-**B**). By immunofluorescence, we verified the localization of BM integrin receptors adjacent to laminin$^+$ BM-like structures at day 25 of organoid differentiation (**Figure 1–figure supplement 1C**). Using transmission electron microscopy and immunoelectron microscopy, we observed advanced podocyte differentiation with primary podocyte processes and confirmed assembly of laminin$^+$ BM structures (**Figure 1D** and **Figure1–figure supplement 2A-B**). We also detected likely endothelial cells present in glomerular structures (**Figure 1B** and **Figure 1–figure supplement 2B**) and a BM-like matrix between podocytes and endothelial cells in day 25 organoid glomeruli (**Figure 1–figure supplement 2A-B**). Together, these findings demonstrate that kidney organoids mimic the normal progression of kidney differentiation with the concomitant assembly of BM structures *in vitro*.

To determine the role of organoids as a model to study abnormal BMs in kidney disease, we investigated iPSC lines from patients with Alport syndrome (AS), a genetic disorder caused by variants in collagen IV genes (Barker et al., 1990). We selected iPSC lines from a mother and son, both carrying a likely pathogenic X-linked missense variant in *COL4A5* (c.3695G>A; p.Gly1232Asp) and a variant of unknown significance in *COL4A4* (c.3286C>T; p.Pro1096Ser; **Figure 1E**; see **Supplementary file 1** and **Supplementary information** for clinical details). AS patient-derived organoids progressed through differentiation and formed $WT1^+$/$NPHS1^+$/$CDH1^+$ glomeruli and $CDH1^+$ tubules, (**Figures 1F** and **Figure 1–figure supplement 3**) with no evident abnormalities by light microscopy. We found comparable distribution of the collagen IV $\alpha4$ chain in AS and wild-type organoids (**Figure 1–figure supplement 3**) confirming assembly of a collagen IV $\alpha3\alpha4\alpha5$ network, which is described in AS patients with missense variants (Yamamura et al., 2020b). Since laminin compensation is reported in X-linked AS (Abrahamson et al., 2007; Kashtan et al., 2001), we examined the deposition of laminin-$\beta2$ (LAMB2) in AS organoids. We found increased LAMB2 in AS organoids, most notable in extra-glomerular BM (**Figure 1G**), and further confirmed increased LAMB2 levels with immunoblotting (**Figure 1H**). Together, these findings demonstrate the potential of kidney organoids to reveal abnormal patterns of BM assembly in human development and disease.

A conserved sequence of BM assembly in kidney organoids

Having identified BM structures in kidney organoids, we next explored the potential for this system to model human BM assembly. Studies in mouse and invertebrate development have shown a sequence of BM assembly with initial laminin deposition followed by incorporation of collagen IV, nidogen and perlecan (Jayadev et al., 2019; Matsubayashi et al., 2017; Urbano et al., 2009). To investigate the assembly sequence in organoids, we used whole-mount immunofluorescence to examine the temporal co-deposition of COL4A1 with laminin (using a pan-laminin antibody), and nidogen with perlecan during differentiation. We found punctate deposits of pan-laminin in interrupted BM networks around cell clusters in day 11 organoids, and in continuous BMs around $CD31^+$ endothelial and epithelial structures in day 18 and 25 organoids (**Figure 2A**). Conversely, COL4A1 was weakly detected in day 11 organoids, partially co-distributed with laminin by day 18, and within continuous BM networks by day 25 (**Figure 2A**). Nidogen and perlecan colocalized in discreet, interrupted BMs in day 11 organoids and later in linear BM networks around tubules and $NPHS1^+$ glomerular structures on day 18 and 25 (**Figure 2B**). Together, these findings indicate that kidney organoids recapitulate the sequence of BM assembly described *in vivo*, reinforcing their fidelity as system for investigating BM dynamics.

Time course proteomics reveals complex dynamics of BM assembly

To understand global BM dynamics, we investigated organoids at day 14, 18 and 25 with time course proteomic analysis. We broadly separated intracellular and extracellular proteins by fractionation (**Figures 3A, 3B and Figure 3–figure supplement 1A**) based on solubility (Lennon et al., 2014). Overall, we detected 5,245 proteins in the cellular fraction and 4,703 in the extracellular fraction (**Supplementary file 2**), and by cross-referencing with the human matrisome (Naba et al., 2016) we identified 228 matrix proteins in kidney organoids (**Figure 3–figure supplement 1B** and **Supplementary file 2**). Principal component analysis highlighted discreet clustering for the organoid time points based on matrix protein abundance (**Figure 3–figure supplement 1C**). There was an increase in matrix abundance from day 14 to 25 (**Figure 3B**) and 203 (~90%) of matrix proteins were detectable at all time points (**Figure 3C**). This initial analysis confirmed a gradual assembly of matrix during organoid differentiation. To address global BM composition, we identified BM proteins using the comprehensive BM gene network (Jayadev et al., 2021) curated in *basement membrane*BASE (https://bmbasedb.manchester.ac.uk/). The organoid extracellular fraction was enriched for BM proteins compared to the cellular fraction (**Figure 3D**), which was expected as these are large, highly cross-linked proteins and hence, difficult to solubilize. Furthermore, we observed an increasing trend for BM protein levels through day 14 to 25 (**Figure 3D**), again indicating BM deposition over time, and corroborating our immunofluorescence findings. In total, we identified 78 BM proteins (**Figure 3E**) including components deposited early in kidney morphogenesis (*e.g.*, COL4A1, COL4A2, LAMA1, LAMB1, LAMC1) (**Figures 3F** and **Figure 3–figure supplement 1D**). LAMA5 and LAMB2, two key components of the mature GBM, only appeared amongst the most abundant BM components at day 25 (**Figure 3–figure supplement 1D**) indicating a temporal expression of GBM laminins during organoid differentiation (**Figure 3F**). This was confirmed by marked upregulation of mature GBM proteins from day 18 to 25, with LAMB2 scoring with the highest fold-change followed by LAMA5 and COL4A3 (**Figures 3G and 3H**). LAMA5 was also enriched from day 14 to 18 together with other GBM proteins (COL4A3, AGRN) and early BM collagens and laminins (COL4A1, COL4A2, LAMC1, LAMA1) (**Figures 3G, 3H** and **Figure 3–figure supplement 1E**).

During GBM assembly, an initial laminin-111 (α1αβ1γ1) network is sequentially replaced by laminin-511 then -521 (Abrahamson et al., 2013). We therefore reasoned that day 14 to 18 would represent a period of intense BM assembly and initial GBM differentiation. In support of this hypothesis, a pathway enrichment analysis of upregulated proteins from day 14 to 18 revealed an overrepresentation of terms associated with BM assembly and remodeling, including laminin interactions, degradation of extracellular matrix (ECM) and collagen chain trimerization (**Figure 3–figure supplement 1F**). Together, this global proteomic analysis revealed new insights into the complexities of BM dynamics and the distinct temporal emergence of BM isoforms required for long term functional integrity of the GBM.

Tracking collagen IV and laminin isoforms during organoid differentiation

To confirm the temporal sequence of specific BM isoforms we investigated the distribution of COL4A1, COL4A3, LAMA5, LAMB1, LAMB2 in organoid BMs through day 14 to 25 by immunofluorescence (**Figure 4D**). As described earlier, COL4A1 appeared on day 11 (**Figure 2A**) and partial colocalization with laminin on day 14, and as continuous BM networks from day 18 (**Figure 4A**). Conversely, COL4A3 was scarce from day 14 to 18, but clearly colocalized with laminin in glomerular structures on day 25 (**Figure 4A**). We detected LAMA5 from day 18 and this increased in glomerular structures at day 25. LAMB1 was widely distributed from day 14 to 25 whereas LAMB2, detected from day 18 onwards, was enriched in glomerular structures at day 25. These findings not only confirm a temporal emergence of specific BM isoforms, but also highlight specific localization to glomerular structures later in differentiation.

We then hypothesized that distinct cell types would express specific BM isoforms to concentrate their distribution and therefore analyzed single-cell RNA sequencing (scRNA-seq) data from day 25 kidney organoids (Combes et al., 2019b) to map the expression profile for BM genes (**Figure 4–figure supplement 1A**, **Supplementary file 3**). We found *NPHS2*$^+$/*PODXL*$^+$ podocytes were the main source of *COL4A3*, *COL4A4* (**Figures 4B** and **Figure 4–figure supplement 1A**) and they also had high levels of expression for *LAMA5* and *LAMB2*. *PECAM1*$^+$/*KDR*$^+$ endothelial cells, *MAB21L2*$^+$/*CXCL14*$^+$ stromal cells and *PAX8*$^+$/*PAX2*$^+$ nephron cell lineages all expressed *COL4A1*, *COL4A2*, *LAMB1*, *LAMC1* and *LAMA1* was detected in the nephron cell cluster whereas LAMA4 was expressed by both endothelial and stroma cells (**Figures 4B and Figure 4–figure supplement 1A**). These findings align with current understanding of kidney development *in vivo* and indicate that kidney organoids recapitulate the known cell specific contributions to BM assembly during glomerulogenesis.

Since the developmental transition from the α1α1α2 to the α3α4α5 network of collagen IV is key for long term GBM function and reduced or absent α3α4α5 leads to loss of function (Miner and Sanes, 1996), we mapped the localization of collagen IV isoforms in day 25 organoids and compared to laser microdissected E19 mouse glomeruli (**Supplementary file 4**). With proteomic analysis we identified 25 BM proteins in the maturing E19 glomeruli and these were also detected in kidney organoids. Identifications included COL4A1, COL4A2 and COL4A3 (**Figure 4C**) thus indicating presence of α1α1α2 and α3α4α5 networks. We compared the localization of COL4A1 and COL4A3 by immunofluorescence in the mouse and NPHS2$^+$ glomeruli in kidney organoids (**Figure 4D**). We observed a similar distribution of COL4A1, but for COL4A3, we found GBM-like and extraglomerular distribution in kidney organoids (**Figure 4D**). Therefore, kidney organoids initiate collagen IV isoform transitions during glomerulogenesis. To further explore mechanisms of transition, we investigated the expression of LIM homeodomain transcription factor 1-beta (LMX1b) and FERM-domain protein EPB41L5 in day 25 organoids (**Figure 4–figure supplement 1B**). LMX1b and EPB41L5 are proposed regulators of GBM assembly and isoform transitions during development (Maier et al., 2021; Morello et al., 2001). Moreover, EPB41L5 is also implicated in regulating the incorporation of laminin-511 and -521, into stable GBM scaffolds. We found that similar cell populations expressed EPB41L5 and LAMA5 (**Figure 4–figure supplement 1B**), and there was an increase in EPB41L5 protein levels from day 14 to 18 (**Figure 4–figure supplement 1C**), coinciding with an increase in LAMA5 (**Figures 3G-H**). Together, these findings demonstrate that kidney organoids initiate isoform transitions during glomerular differentiation, with the expression of known BM regulators.

BMs in late-stage organoids and fetal kidneys are highly correlated

To relate BM assembly in organoids to a comparable *in vivo* system, we examined whole fetal kidneys. Having verified morphological similarity between day 25 organoids and E19 mouse fetal kidney (**Figure 1C**), we used this timepoint for comparison by proteomic analysis. We generated cellular and extracellular fractions from whole fetal kidneys (**Figures 5A**, **Figure 5–figure supplement 1A-B**) and identified 208 matrix components from a total of 5,071 proteins (**Figure 5A**; **Supplementary file 4**). These included 83 BM proteins and the most abundant were those seen early (COL4A1, COL4A2, COL18A1, LAMB1, LAMC1) and later (LAMA5) in BM assembly (**Figure 5–figure supplement 1C**). We compared these findings to a proteomic dataset from the E18.5 mouse kidney (Lipp et al., 2021), and found considerable overlap, with a further 130 matrix protein identifications (**Figure 5C**), including key GBM components COL4A3, COL4A4, COL4A5 and COL4A6. We then compared the BM proteins from each organoid timepoint with E19 mouse kidneys (**Figure 5D**) and found the highest overlap (58.4%) between E19 and day 25 kidney organoids. In line with previous findings (Hale et al., 2018), this comparison highlighted later expression of TINAG and TINAGL1 in day 25 organoids, also detected in E19 mouse kidneys but not in day 14 or day 18 organoids. TINAGL1 was also detected in E19 mature glomeruli (**Figure 4C**) and in proteomic studies of adult human glomeruli (Lennon et al., 2014) but its role for BM biology remains unknown. In addition, the overlap for other structural and matrix-associated proteins was lower than for BM proteins (**Figure 5–figure supplement 1D**), which highlights conservation of BM composition between mouse and kidney organoids. To further verify similarities, we performed a Spearman's rank correlation and found E19 had the higher correlation with more differentiated organoids (**Figures 5E** and **Figure 5–figure supplement 1E**).

Next we analyzed scRNA-seq datasets from E18.5 mouse kidneys (Combes et al., 2019a); **Figure 5F**) and from 8- and 9-wpc human kidneys (Young et al., 2018) (**Figure 5–figure**

supplement 2) to identify cells expressing specific BM genes (**Supplementary file 3**). In the mouse we found mature GBM components expressed by *Synpo*$^+$/*Nphs2*$^+$ podocytes (*Col4a3*, *Col4a4*, *Lama5*, *Lamb2*), *Plvap*$^+$/*Pecam1*$^+$ vascular cells (*Lama5*, *Lamb2*), and *Cited1*$^+$/*Crym*$^+$ nephron progenitor cell lineages, and *Aldob*$^+$/*Fxyd2*$^+$ tubular, vascular and *Six2*$^+$ stromal cells predominantly contributing with *Col4a1*, *Col4a2*, *Lamb1* and *Lamc1* expression (**Figure 5F**). Lama1 was mainly expressed by *Clu*$^+$/*Osr2*$^+$ S-shaped bodies and *Gata3*$^+$/*Wfdc2*$^+$ ureteric bud/distal tubular cells, and *Lama4* restricted to vascular and stromal cells. A similar pattern was observed in the embryonic human kidney (**Figure 5–figure supplement 2**), and these findings were also consistent with our findings in day 25 kidney organoids (**Figure 4B** and **Figure 4–figure supplement 1**). Interestingly, immune cells also contributed for *Col4a1* and *Col4a2* expression in both mouse and human kidneys. Collectively, these findings highlight the conservation of BM gene expression across organoids and fetal kidneys.

Basement membranes are dynamic through embryonic development to adulthood

Having observed dynamic BM composition during kidney development we then compared composition in adulthood. For this, we analyzed proteomic data from isolated adult human nephron compartments and identified 71 glomerular BM proteins, and 61 in the tubulointerstitium (**Supplementary file 6**). We compared BM networks in the adult kidney with both developmental systems (day 25 kidney organoids and E19 mouse kidney) and found a significant overlap with 44 of 107 BM proteins shared amongst all datasets. These included core components (COL4A1, COL4A2, LAMA1, LAMB1, LAMC1, HSPG2, COL18A1, NID1, NID2), mature GBM components (COL4A3, COL4A5, LAMA5, LAMB2) and many minor structural proteins (**Figure 6A**). We found a strong correlation between both matrix and BM networks in glomerular and tubulointerstitial compartments, but lower correlation between adult and developmental datasets (**Figures 6B** and **Figure 6–figure supplement 1**). Interestingly, the correlation between adult and development data was lower for BM than for all matrix proteins, suggesting that although kidney BMs retain a consistent profile through development to adulthood, there is diversification within distinct kidney compartments.

To understand cellular origins of BM components through development to adulthood, we analyzed adult human kidney scRNA-seq data (Young et al. 2018; **Supplementary file 3**), and as with organoids and mouse fetal kidney, we found *COL4A1*, *COL4A2*, *LAMB1* and *LAMC1* predominantly expressed by endothelial and tubular cells. Although podocyte markers were not enriched in the adult dataset, we detected *COL4A3* and *COL4A4* expression by *PAX8*$^+$ nephron cell types, and *LAMA5* and *LAMB2* mainly expressed by *KRT5*$^+$/*EMCN*$^+$ endothelial cells (**Figure 6C**). *LAMA4* was widely detected in both E18.5 mouse kidney and day 25 organoids (**Figures 3B, 4F** and **Figure 4–figure supplement 1**), but barely present in the adult kidney (**Figure 6C**), consistent with previous reports of transient expression in human kidney development (Miner, 1999). These findings demonstrate consistent cellular origins for BM components through development to adulthood.

To further verify the extent of this consistency, we selected minor BM components across all scRNA-seq datasets (**Figure 6D**). These included: *FBLN1* and *TGFBI* both implicated in BM remodeling (Boutboul et al., 2006; Feitosa et al., 2012); *FRAS1* and *FREM2* important for branching morphogenesis (Chiotaki et al., 2007; Petrou et al., 2008); and *TINAG* and *TINAGL1*, with unknown roles in BM function. We found a common pattern of enrichment amongst the developmental datasets for *FBLN1*, which was expressed by stromal cells; *FRAS1* and *FREM2* were expressed by podocyte and nephron cell clusters; and *TGFBI* by stromal cells, nephron progenitors, and by immune cells. In human adult kidneys *FBLN1* was mainly present in pelvic epithelial cells and *FRAS1*/*FREM2* in ureteric bud/distal tubule cells, thus indicating spatiotemporal expression of these components. *TINAG* and *TINGAL1* had variable patterns of cell expression across datasets. This comparative analysis shows conservation of distinct cell types contributing to BM assembly during kidney development and uncovers diversification in cellular origins of BM components in adult kidneys.

DISCUSSION

Mammalian kidney development involves a series of morphogenetic events that proceed in an orchestrated manner to give rise to ~1,000,000 nephrons in the human kidney and 1000's in the mouse. Many of these processes require spatiotemporal assembly and remodeling of BMs throughout nephrogenesis (**Figure 7**). Here we demonstrate the fidelity of kidney organoids as a system for investigating assembly and regulation of kidney BMs in health and disease with the following key findings: 1) the identification of a conserved sequence of BM component assembly during kidney organoid differentiation, 2) evidence of global BM dynamics during organoid differentiation with high correlation to fetal kidney BM composition and 3) the diversification of the cellular origin of BM components during kidney development.

BMs are complex structures and proteomic studies have highlighted this complexity in homeostasis and disease (Lennon et al., 2014; Randles et al., 2015). During development, BMs are also highly dynamic and undergo intense remodeling (Kyprianou et al., 2020) but understanding of BM assembly and regulation is limited by lack of appropriate systems to track components that are spatiotemporally regulated and undergoing turnover (Naylor et al., 2020). Human fetal tissue has limited availability and studies are restricted to static time points and the technical limitations of imaging in mouse models also impairs investigation of the dynamic BM environment *in vivo*. However, BM studies in *Drosophila* and *C. elegans* have provided important insights into BM dynamics and turnover using fluorescent tagging of endogenous proteins (Keeley et al., 2020; Matsubayashi et al., 2020) and these studies highlight the power of studying BM dynamics.

Despite the developmental limitations with iPSC-derived kidney organoids, including lack of directional cues, vascularization, and cortical-medullary segmentation (Romero-Guevara et al., 2020), this system has morphological and molecular features comparable to fetal kidney tissue that overcome species differences and provides a complex *in vitro* environment to examine BM assembly (Bantounas et al., 2018). We demonstrated that kidney organoids differentiate into glomerular structures containing the cells required for GBM assembly and single-cell transcriptomic studies have also shown over 20 other distinct cell populations in kidney organoids (Combes et al., 2019a; Wu et al., 2018). Cross-talk between different cell types is essential for BM assembly and influences composition (Byron et al., 2014) hence, the multiple cell types in the organoid system enable BM formation and remodeling. A key finding from this study is that organoids form BMs early during differentiation, and more importantly, recapitulate a sequence of assembly events with initial deposition of laminin followed by incorporation of collagen IV, nidogen and perlecan (Brown et al., 2017; Sasaki et al., 2004).

Kidney organoids have also provided new insights into disease processes (Rooney et al., 2021; Tanigawa et al., 2018; Tian and Lennon, 2019). We found that organoids with a pathological missense variant in *COL4A5* differentiated and deposited core BM proteins, including a collagen IV $\alpha3\alpha4\alpha5$ network, which is described in missense variants. In one study 64 out of 146 patients with X-linked Alport syndrome had the collagen IV $\alpha5$ chain in the GBM (Yamamura et al., 2020a). Despite evidence of protein secretion, the GBM fails to maintain function in these patients. Interestingly, we found increased deposition of LAMB2 in extraglomerular BMs in Alport organoids. Dysregulation of glomerular laminins, including LAMB2, in patients with Alport syndrome and animal models has been reported (Abrahamson et al., 2007; Kashtan et al., 2001), but the mechanisms are unclear. Our findings in Alport organoids demonstrate the utility of this system to dissect abnormal mechanisms of BM assembly.

To define global BM composition in kidney organoids we used MS-based proteomics and identified 78 BM proteins dynamically expressed throughout the differentiation time course. Core GBM components including laminin-521 and collagen IV α3α4α5, which only appear in mature glomeruli, were also detected. Developmental isoform transitions in the GBM involving laminin and collagen IV are described in humans and rodents (Abrahamson and St John, 1993) and in current understanding, immature glomeruli assemble a primary GBM containing laminin-111 and collagen IV α1α2α1 that is later replaced by laminin-521 and collagen IV α3α4α5 in mature glomeruli. In keeping with these observations, we found a temporal and spatial emergence of mature collagen IV and laminin isoforms within glomerular structures in kidney organoids, and in scRNA-seq data we confirmed podocyte expression of mature GBM markers. These findings demonstrate that kidney organoids can efficiently recapitulate the spatiotemporal emergence of GBM components. The triggers for isoform switching remains unknown but two regulators, LMX1b and EPB41L5, have been implicated. Studies in *Lmxb1* knockout mice suggest that podocyte expression of this transcription factor is not essential for initial GBM assembly but linked to *Col4a3*/*Col4a4* expression during glomerulogenesis as demonstrated by reduced collagen IV α3α4α5 network in the GBM in null *Lmxb1* newborn mice (Morello et al., 2001). We found podocyte specific expression of *LMX1b*/*COL4A3*/*COL4A4* in day 25 kidney organoids, and moreover, confirmed deposition of COL4A3/COL4A4 in a GBM pattern within NPHS2$^+$-glomerular structures in organoids. In addition, podocyte expression of EPB41L5, a component of the podocyte integrin adhesion complex, was linked to GBM assembly *in vivo* and incorporation of laminin-511/521 into extracellular BM networks *in vitro* (Maier et al., 2021). In this study, we detected EPB41L5 in organoid and mouse proteomic datasets, with cell expression patterns matching LAMA5, indicating the potential for this system to unravel further insights into GBM regulation.

There are few proteomic studies addressing the spatiotemporal changes in BM during development. One study of mouse kidney development, defined the global ECM composition through development to adulthood and described a sequence of changes in interstitial matrix over development (Lipp et al., 2021). With our sample fractionation strategy and analytical pipeline, we detected a further 130 matrix proteins, including key GBM components (COL4A3, COL4A4, COL4A5, COL4A6) and BM regulators such as PAPLN and HMCN1 (Keeley et al., 2020; Morrissey et al., 2014). Our findings further demonstrated that late-stage kidney organoids (at day 25) and mouse kidneys on E19 share a very comparable BM profile. We also verified similar patterns of BM gene expression between kidney organoids and fetal human and mouse kidneys, especially for collagen IV and laminin isoforms. Overall, these data demonstrate the high-fidelity with which kidney organoids recapitulate BM gene expression and protein composition seen *in vivo*. Thus, we conclude that kidney organoids are a highly tractable model that can be used to study the dynamic nature of human BM assembly in both health and disease.

MATERIALS AND METHODS

Key Resources Table				
Reagent type (species) or resource	**Designation**	**Source or reference**	**Identifiers**	**Additional information**
strain, strain background (*Mus musculus*)	*Swiss*	University of São Paulo (Brazil)	-	2-months old, male and female mice
cell line (*Homo sapiens*)	iPSC	HipSci	CGAP-38728; CGAP-4852B; CGAP-581E8	Derived from patients with Alport syndrome
cell line (*Homo*	iPSC	Wood et al., 2020	-	Derived from

sapiens)				peripheral blood mononuclear cells
biological sample (*Homo sapiens*)	Embryonic and fetal kidneys	Joint MCR/ Wellcome Trust HDBR	Kidney_ID: 13878; 11295; 13891; 13842; 1358	FFPE samples
antibody	anti-CD31, clone 89C2 (Mouse monoclonal)	Cell Signalling	Cat#: 3582	IF (1:100) WM (1:100)
antibody	anti-E-cadherin, clone M168 (Mouse monoclonal)	Abcam	RRID:AB_1310159	IF (1:300) WM (1:300)
antibody	anti-WT1, clone C-19 (Rabbit polyclonal)	Santa Cruz Biotechnology	RRID:AB_632611	IF (1:100) WM (1:100)
antibody	anti-human nephrin (Sheep polyclonal)	R&D Systems	RRID:AB_2154851	IF (1:200) WM (1:400)
antibody	anti-human collagen IV α1 chain NC1 domain, clone H11 (Rat monoclonal)	Chondrex	Cat#: 7070	IF (1:100) WM (1:400)
antibody	anti-human collagen IV α3 chain NC1 domain, clone H31 (Rat monoclonal)	Chondrex	Cat#: 7076	IF (1:100)
antibody	anti-human collagen IV α4 chain NC1 domain,	Chondrex	Cat#: 7073	IF (1:100)

	clone H43 (Rat monoclonal)			
antibody	anti-human collagen IV α3 chain NC1 domain, clone H63 (Rat monoclonal)	Chondrex	Cat#: 7074	IF (1:50)
antibody	anti-laminin (Rabbit polyclonal)	Abcam	RRID:AB_298179	IF (1:250) Wm (1:250)
antibody	anti-nidogen, clone 302117 (Mouse monoclonal)	Invitrogen	RRID:AB_2609420	IF (8.3 μg/ml) WM (8.3 μg/ml)
antibody	anti-perlecan, clone A7L6 (Rat monoclonal)	Millipore	RRID:AB_10615958	IF (1:250) WM (1:250)
antibody	anti-laminin α5 chain, clone 4C7 (Mouse monoclonal)	Abcam	RRID:AB_443652	IF (1:100)
antibody	anti-laminin β1 chain, clone 4E10 (Mouse monoclonal)	Millipore	RRID:AB_571039	IF (1:100)
antibody	anti-laminin S/laminin β2 chain, clone CL2979 (Mouse monoclonal)	Novus Biologicals	Cat#: NBP-42387	IF (1:50) WB (1:1000)

antibody	anti-podocin (Rabbit polyclonal)	Millipore	RRID:AB_261982	IF (1:200)
antibody	anti-NPHS2 (Rabbit polyclonal)	Abcam	RRID:AB_882097	IF (1:200)
antibody	anti-integrin β1 chain, clone 9EG7 (Rat monoclonal)	(Lenter et al., 1993)	-	IF (1:100)
antibody	anti-rat IgG conjugated with Alexa Fluor 488 (Donkey)	Invitrogen Antibodies	RRID:AB_141709	IF (1:400)
antibody	anti-rat IgG conjugated with Alexa Fluor 594 (Donkey)	Invitrogen Antibodies	RRID:AB_2535795	IF (1:400)
antibody	anti-mouse IgG conjugated with Alexa Fluor 488 (Donkey)	Invitrogen Antibodies	RRID:AB_141607	IF (1:400)
antibody	anti-mouse IgG conjugated with Alexa Fluor 594 (Donkey)	Invitrogen Antibodies	RRID:AB_141633	IF (1:400)
antibody	anti-rabbit IgG conjugated with Alexa Fluor 488 (Donkey)	Invitrogen Antibodies	RRID:AB_2535792	IF (1:400)
antibody	anti-rabbit IgG conjugated with Alexa Fluor 647	Invitrogen Antibodies	RRID:AB_2536183	IF (1:400)

	(Donkey)			
antibody	anti-rabbit IgG conjugated with Alexa Fluor 594 (Goat)	Invitrogen Antibodies	RRID:AB_141359	IF (1:400)
antibody	anti-sheep IgG conjugated with Alexa Fluor 594	Invitrogen Antibodies	RRID:AB_2758365	IF (1:400)
antibody	anti-sheep IgG conjugated with Alexa Fluor 680	Invitrogen Antibodies	RRID:AB_1500713	IF (1:400)
antibody	anti-mouse IgG DyLight 800 4X PEG conjugated (Goat)	Cell Signaling Technology	RRID:AB_10697505	WB (1:1000)
antibody	anti-rabbit IgG labelled with 10-nm gold (Goat)	Abcam	RRID:AB_954434	Immunogold (1:400)
chemical compound, drug	CHIR99021	Tocris Bioscience	4423/10	-
chemical compound, drug	FGF-9	Peprotech	100-23	-
chemical compound, drug	Heparin	Sigma Aldrich	H3393	-
chemical compound, drug	TeSR™-E8 medium	STEMCELL ™	05991; 05992	-

chemical compound, drug	STEMdiff™ APEL™2 medium	STEMCELL ™	05270	-
software, algorithm	Proteome Discoverer v.2.3.0.523	Thermo Fisher Scientific	RRID:SCR_014477	-

Human fetal kidney

Formaldehyde-fixed paraffin-embedded (FFPE) human fetal kidney sections were provided by the Joint MRC/Wellcome Trust Human Developmental Biology Resource (HDBR) (http://hdbr.org). The HDBR obtains written consent from the donors and has ethics approval (REC reference: 08/H0712/34+5) to collect, store and distribute human material sampled between 4- and 21-weeks post conception. All experimental protocols were approved by the Institute’s Ethical Committee (reference 010/H0713/6) and performed in accordance with institutional ethical and regulatory guidelines.

Induced pluripotent stem cells

Human induced pluripotent stem cells (iPSCs) derived from peripheral blood mononuclear cells (PBMCs) of a healthy individual were generated as previously described (Wood et al., 2020). Whole blood PBMCs were isolated using a Ficoll-Paque (GE17-1440, GE Healthcare) and grown in StemSpan Erythroid Expansion Medium (02692, Stem Cell Technologies) for 8 days before being transduced using CytoTune-iPS 2.0 Sendai virus (A16517, Invitrogen) and grown on vitronectin (A14700, Gibco) coated plates in ReproTeSR medium (05926, Stem Cell Technologies). When large enough, colonies were manually isolated and grown in TeSR-E8 medium (05991, STEMCELL). iPSCs derived from patients with Alport syndrome (see **clinical presentation** below) were generated at the Wellcome Sanger Institute, in collaboration with the Human Induced Pluripotent Stem Cell Initiative (HipSci, www.hipsci.org; (Kilpinen et al., 2017). Following ethical approval (REC Reference

11/H1003/3) and patient consent, dermal fibroblasts were obtained from skin biopsies and programmed to iPSC. For this study, we investigated three members of the same family: a male index patient and his mother carrying a likely pathogenic *COL4A5* variant (c.3695G>A; p.Gly1232Asp, PM1_strong, PM2_moderate, PM5_moderate, PP3_moderate, posterior probability 0.988) and a *COL4A4* variant of uncertain significance (c.3286C>T; p.Pro1096Ser, PM2_moderate, PP3_moderate, posterior probability 0.5), and his sister carrying only the *COL4A5* variant. All human cell lines have been authenticated using short tandem repeat profiling. All experiments were performed with mycoplasma-free cells.

Clinical presentation

The male index patient, aged 4, presented with recurrent episodes of macroscopic hematuria and persistent microscopic haematuria and his mother also exhibited microscopic hematuria. He underwent a kidney biopsy, which had normal appearances by light microscopy and immunohistochemical analysis did not show glomerular deposition of immuno-reactants. With electron microscopy the glomerular basement membrane (GBM) was thinned in some glomerular capillary loops. In one or two others the GBM was irregularly thickened with lamination. There were also electron-lucent lacunae between the laminations, some of which contained electron-dense regions and the ultrastructural changes, in combination with the highly suggestive presentation and family history, confirmed a diagnosis of Alport Syndrome. The patient subsequently developed hypertension and was treated with antihypertensive medications, including renin-angiotensin system blockade, and exhibited slow decline in his kidney function. He eventually progressed to end stage kidney disease and received a pre-emptive kidney transplant from his healthy father at the age of 19. Subsequent genetic testing identified a likely pathogenic missense variant in *COL4A5* (c.3695G>A; p.Gly1232Asp) and a variant of unknown significance in *COL4A4* (c.3286C>T; p.Pro1096Ser). Further genetic testing in the family confirmed that both the patient’s mother and sister carried one or both variants. His mother had both the *COL4A5* and *COL4A4* variants and exhibited persistent microscopic hematuria and urine protein:creatinine ratios (uPCR) ranging from 17 to 30 mg/mmol and estimated glomerular filtration rate steady between 74 to 85 ml/min/1.73m^2 body surface area over 5 years to most recent follow-up aged 55. The index patient's sister shared only the *COL4A5* variant and exhibited persistent hematuria with proteinuria (uPCR 264 mg/mmol falling to 45-89 mg/mmol on institution of renin-angiotensin system blockade aged 25). Serum creatinine was normal with eGFR >90 ml/min/1.73m^2 body surface area at last follow-up aged 30. The *COL4A4* variant was also detected in the index case's healthy maternal grandmother (in whom urinalysis was normal) but the *COL4A5* variant was absent from both maternal grandparents, suggesting a *de novo* variant in his mother. Pathogenicity was assessed following ACMG coding criteria (*COL4A5* variant: PM1_STR, PM2_MOD, PM5_MOD, PP3_MOD; *COL4A4* variant: PM2_MOD, PP3_MOD).

Kidney organoid differentiation

We differentiated human iPSCs (**Supplement file 1**) to kidney organoids as previously described (Takasato et al., 2015). iPSCs were maintained at 37 °C in TeSR™-E8 medium with 25x Supplement (05991, 05992, STEMCELL) in 6-well plates (3516, Corning) coated with vitronectin (A14700, Gibco). Prior to differentiation (day 0) cells were dissociated with TrypLE (12563029, Thermo Fisher Scientific), counted with a hemocytometer and seeded in vitronectin-coated 24-well plates (3524, Corning) at a density of 35,000 cells/cm^2 in TeSR™-E8™ medium with Revitacell 10 µl/ml (A2644501, Gibco). Intermediate mesoderm induction was performed by changing medium after 24 hours to STEMdiff™ APEL™2 (05270, STEMCELL™) with 3% protein free hybridoma medium (12040077, Gibco) and 8 µM CHIR99021 (4423/10, Tocris Bioscience) for 4 days. On day 5, CHIR99021 was replaced by 200 ng/ml FGF-9 (100-23, Peprotech) and 1 µg/ml Heparin (H3393, Sigma Aldrich). On Day 7, cells were dissociated with TrypLE, counted, and pelletized into organoids (250,000 cells each) by centrifuging them at 400x g/min four times. Organoids were carefully placed on 0.4

µm Millicell Cell Culture Insert in 6-well plates (PICM0RG50, Millipore), and cultured for 1 hour in APEL™2 medium with 5 µM CHIR99021 and subsequently in APEL™2 medium supplemented with 200 ng/mL FGF9 and 1 µg/mL Heparin until Day 11. From day 12, organoids were grown in STEMdiff™ APEL™2 without growth factors, with medium changed at every 2 days.

Mice

All mouse handling and experimental procedures were approved by the Animal Ethics Committee of the Institute of Biomedical Sciences (ICB) - University of São Paulo (USP), Brazil; reference 019/2015). Two-month-old *Swiss* female mice were housed in an experimental animal facility (ICB, USP) kept in groups of 3-4 subjects per cage (41x34x16 cm) at 12-hour light/dark cycle at 25 °C, with free access to water and chow. Mating occurred overnight, and females were checked for vaginal plugs on the next morning to determine if mating had occurred and gestation was timed accordingly (embryonic day 1). Pregnant dams were separate and kept in individual cages (30x20x13 cm) under the same conditions mentioned previously. Fetuses were collected on the embryonic day 19 (E19), following C-section surgery in the pregnant mice under anesthesia with 25 mg/kg avertin (T48402, Sigma-Aldrich). Fetal kidneys were dissected and processed for histological analysis, or snap-frozen in liquid nitrogen for proteomic analysis.

Whole mount immunofluorescence

Whole organoids were fixed with 2% (wt/vol) paraformaldehyde at 4 °C for 20 minutes, washed with Phosphate Buffered Saline (PBS; D8537, Sigma-Aldrich) and blocked with 1x casein blocking buffer (B6429, SigmaAldrich) for 2 hours at room temperature. Samples were incubated at 4 °C overnight with primary antibodies diluted in blocking buffer. After thoroughly washing with 0.3% (vol/vol) Triton X-100 in PBS, the samples were incubated at 4 °C overnight with Alexa Fluor-conjugated secondary antibodies. Nuclei were stained with HOECHST 33342 solution (B2261, SigmaAldrich). Samples were mounted in glassbottomed dishes (P35G-1.5-10-C, MatTek) with ProLong Gold Antifade mountant (P36934, Invitrogen), and imaged with a Leica TCS SP8 AOBS inverted confocal microscope, using hybrid detectors with the following detection mirror settings: FITC 494-530 nm; Texas red 602-665 nm; Cy5 640-690 nm. When it was not possible to eliminate fluorescence crosstalk, the images were collected sequentially. When acquiring 3D optical stacks, the confocal software was used to determine the optimal number of Z sections. Only the maximum intensity projections of these 3D stacks are shown in the results. 3D image stacks were analyzed with ImageJ v 1.53g software (Rasband, W.S., ImageJ, U. S. National Institutes of Health, Bethesda, Maryland, USA; available at https://imagej.nih.gov/ij/, 1997-2018).

Histology and immunofluorescence

For light microscopy, FFPE sections were stained with hematoxylin and eosin (H&E) for morphological analysis. Images were acquired on a 3D-Histech Pannoramic-250 microscope slide-scanner (Zeiss) using the Case Viewer software (3D-Histech). For immunofluorescence microscopy, either cryosections or FFPE were subjected to nonspecific binding site blocking with 10% normal donkey serum in 1% BSA/PBS, and treated with primary and secondary antibody solutions (see **Key Resources Table**). FFPE samples were submitted to heat-induced antigen retrieval with 10 mM sodium citrate buffer (pH 6.0) in a microwave for 15 min and treated with 0.1M glycine/6M urea solution for 30 minutes at room temperature prior to blocking. The slides were mounted and analyzed with a Zeiss Axioimager.D2 upright microscope equipped with a Coolsnap HQ2 camera (Photometrics). Images were acquired with the Micromanager Software v1.4.23 and processed using ImageJ.

Electron microscopy

Whole mount primary antibody labelling was performed as described above. After overnight incubation at 4 °C with a rabbit pAb anti-laminin antibody (ab11575, Abcam), organoids were washed with PBS-Triton and incubated overnight at 4 °C with a goat anti-rabbit IgG labelled with 10nm gold (ab39601, Abcam) diluted 1:400. Samples were then fixed with 4% paraformaldehyde and 2.5% (wt/vol) glutaraldehyde (Agar Scientific, UK) in 0.1 M HEPES (H0887, SigmaAldrich) pH 7.2, and postfixed with 1% osmium tetroxide (R1024, Agar Scientific) and 1.5% potassium ferrocyanide (214022, The British Drug House, Laboratory Chemicals Division) in 0.1M cacodylate buffer (pH 7.2) (R1102, Agar Scientific) for 1 hour, then with 1% uranyl acetate (R1100A, Agar Scientific) in water for overnight. Samples were dehydrated, embedded with low viscosity medium grade resin (T262, TAAB Laboratories Equipment Ltd) and polymerized for 24 hours at 60 °C. For transmission EM, sections were cut with Reichert Ultracut ultramicrotome and observed with FEI Tecnai 12 Biotwin microscope at 80kV accelerating voltage equipped a Gatan Orius SC1000 CCD camera.

SDS-PAGE and immunoblotting

Organoid samples were homogenized in ice cold Pierce™ IP Lysis Buffer Proteins (87787, ThermoFisher) supplemented with EDTA-free protease inhibitor cocktail (04-693-159-001, Roche) to extract proteins. Following, proteins were resolved by SDS-PAGE in a NuPAGE 4-12% Bis-Tris gel (NP0322, Invitrogen) and wet-transferred to nitrocellulose membrane (Z612391, Whatman). Gel loading was assessed by Ponceau S staining (P7170, SigmaAldrich). Membranes were blocked with Odyssey blocking buffer (927-40000, LI-COR) for 1 hour, and were probed with specific primary and secondary antibodies (see **Key Resources Table**) diluted in Tris-buffered saline soliton (TBS). Protein bands were visualized using the Odyssey CLx imaging system (LI-COR Biosciences), and background-corrected band optical densitometry was determined using ImageJ.

Sample enrichment for proteomics analysis

Kidney organoids samples (days 14, 18 and 25 of differentiation) were pooled accordingly (*n*=3 pools per time point), and E19 mouse fetal kidneys (*n*=6) were enriched for matrix proteins as previously described (Lennon et al., 2014). Briefly, samples were manually homogenized and incubated in a Tris-buffer (10 mM Tris pH 8.0, 150 mM NaCl, 25 mM

EDTA, 1% Triton X-100 and EDTA-free protease inhibitor cocktail) for 1 hour to extract soluble proteins. The supernatant (fraction 1) was collected by centrifuging (at 14,000x *g* for 10 min) and the remaining pellet was resuspended in an alkaline detergent buffer (20 mM Na_4OH, 0.5% in PBS-Triton) and incubated for 1 hour to solubilize and disrupt cell-matrix interactions. The supernatant (fraction 2) was collected by centrifugation and the pellet treated with 0.4 µg Benzonase (E1014-25KU, Sigma-Aldrich) in PBS (D8537, Sigma-Aldrich) for 30 min at room temperature to remove DNA/RNA contaminants. After inactivating Benzonase at 65 °C for 20 min, samples were centrifuged and the remaining pellet was resuspended in a 5x reducing sample buffer (100 mM Tris pH 6.8, 25% glycerol, 10% SDS, 10% β-mercaptoethanol, 0.1% bromophenol blue) to yield the ECM fraction. Fractions 1 and 2 were combined (1:1) into a cellular fraction.

Laser microdissection microscopy

E19 mouse kidneys (*n*=4) were embedded in OCT for cryosectioning. 10-μm-thick cryosections were acquired and placed onto MMI membrane slides (50102, Molecular Machines and Industries), fixed with 70% ethanol and stained with haematoxylin and eosin to allow visualization of maturing mouse glomeruli using a 40x/0.5 FL N objective. 150 glomeruli (per samples) were laser dissected around the Bowman's capsule using an Olympus IX83 Inverted fluorescence snapshot microscopy equipped with MMI CellCut Microdissection system and the MMI CellTools software v.5.0 (Molecular Machines and Industries). Laser settings were speed = 25 μm/s, focus = 16.45 μm, power = 72.5%. Sections were collected onto sticky 0.5 ml microtube caps (Molecular Machines and Industries) and stored at -80°C.

Trypsin digestion

For in-gel digestion, protein samples from E19 mouse kidneys were briefly subjected to SDS-PAGE to concentrate proteins in the gel top, and stained with Expedeon InstantBlue

(Z2, Fisher Scientific). After distaining, gel-top protein bands were sliced and transferred to a V-bottomed perforated 96-wells plate (Proxeon) and incubated with 50% acetonitrile (ACN) in digestion buffer (25 mM $NaHCO_3$) for 30 min at room temperature. After centrifuging (1500 rpm for 2 min), gel pieces were shrunk with 50% ACN and completely dried by vacuum centrifugation for 20 min at -120 °C. After rehydrating gel pieces, proteins were reduced with 10 mM dithiothreitol (DTT; D5545, Sigma-Aldrich) in digestion buffer for 1 hour at 56 °C and alkylated with 55 mM iodoacetamide (IA; I149, Sigma-Aldrich) in digestion buffer for 45 min at room temperature in the dark and spun down. Gel pieces were shrunk with alternating 100% ACN and dried by vacuum centrifugation. Protein digestion with 1.25 ng/l trypsin (V5111, Promega) was carried out at 37 °C overnight, followed by centrifugation to collected the resulting peptides. Finally, samples were dried by vacuum centrifugation and resuspended in 50% ACN in 0.1% formic acid. For in-solution digestion, samples were sonicated in lysis buffer (5% SDS in 50 mM TEAB pH 7.5) using a Covaris LE220+ Focused Ultrasonicator (Covaris), reduced with 5 mM DTT for 10 min at 60 °C and alkylated with 15 mM IA for 10 min at room temperature in the dark. After quenching residual alkylation reaction with 5 mM DTT, samples were spun down, acidified with 1.2% formic acid and transferred to S-Trap Micro Spin columns (Protifi). Contaminants were removed by centrifugation, and protein digestion with 0.12 g/l trypsin (in 50 mM TEAB buffer) was carried out 1 hour at 47 °C. Trapped peptides were thoroughly washed with 50 mM TEAB, spun down, washed with 0.1% formic acid, and eluted from the S-trap columns with 30% ACN in 0.1% formic acid solution.

Offline peptide desalting

Peptide samples were incubated with 5.0 mg Oligo^{TM} R3 reverse-phase beads (1133903, Applied Biosystems) in 50% ACN in a 96-well plate equipped with 0.2 m polyvinylidene fluoride (PVDF) membrane filter (3504, Corning). After centrifuging, the bead-bound peptides were washed twice with 0.1% formic acid, spun down and eluted with 30% ACN in 0.1% formic acid. Retrieved peptides were dried by vacuum centrifugation and sent to the

Bio-MS Core Research Facility (Faculty of Biology, Medicine and Health, University of Manchester) for mass spectrometry analysis.

Mass spectrometry data acquisition and analysis

Peptide samples were analyzed by liquid chromatography (LC)-tandem mass spectrometry using an UltiMate® 3000 Rapid Separation LC (RSLC, Dionex Corporation, Sunnyvale, CA) coupled to a Q Exactive™ Hybrid Quadrupole-Orbitrap™ (Thermo Fisher Scientific, Waltham, MA) mass spectrometer. Peptides were separated on a CSH C18 analytical column (Waters) using a gradient from 93% A (0.1% formic acid in water) and 7% B (0.1% formic acid in ACN) to 18% B over 57 min followed by a second gradient to 27% B over 14 min both at 300 nl/min. Peptides were selected for fragmentation automatically by data dependent acquisition. Raw spectra data were acquired and later analyzed using Proteome Discoverer software v.2.3.0.523 (Thermo Fisher Scientific). MS data was searched against SwissProt and TrEMBL databases (v. 2018_01; OS = *Mus musculus* for mouse samples; OS=*Homo sapiens* for kidney organoids) using SEQUEST HT and Mascot search tools. Tryptic peptides with $\leq$ 1 missed cleavage were considered for the search, and mass tolerance for precursor and fragment ions were 10 ppm and 0.02 Da, respectively. Carbamidomethylation of cysteine was as fixed modification, oxidation of methionine, proline and lysine, and N-terminal acetylation as dynamic modifications. False discovery rate (FDR) for peptide/protein identifications was set to 1%, and protein validation was performed using Target/Decoy strategy. Label-free protein abundances were determined based on precursor ion intensity, and relative changes in protein abundance by calculating abundance ratios accordingly. Results were filtered for significant FDR master proteins identified with $\geq$ 1 unique peptide detected in 2/3 of replicates. The mass spectrometry proteomics data have been deposited to the ProteomeXchange Consortium via the PRIDE partner repository (Perez-Riverol et al., 2019) with the dataset identifiers: PXD025838, PXD025874, PXD025911 and PXD026002.

Enrichment and interactome analyses

Gene ontology (GO) enrichment analysis was performed using the DAVID bioinformatics resource v.6.8 ((Huang et al., 2009); available at https://david.ncifcrf.gov), and term enrichment was determined through Fisher's exact test with Benjamini-Hochberg correction, with a term selected as enriched when FDR < 0.1. Pathway enrichment was performed for proteins differentially expressed using the Reactome database ((Jassal et al., 2020); available at https://reactome.org/). To generate interactome figures, a list of proteins was uploaded to STRING v.11.0 (Szklarczyk et al., 2015) to obtain a collection of high confident protein-protien interactions (combined score $\geq$ 70%), which was further uploaded into Cytoscape v.3.8.1 (Shannon et al., 2003) to customize the interactomes.

Single cell RNA-sequencing analysis

We selected three published single cell-RNA sequencing datasets generated from kidney organoids (GSE114802), fetal and adult human kidneys (EGAS00001002325, EGAS00001002553), and fetal mouse kidney (GSE108291) to identify the cellular origins of BM genes. We first removed the low-quality cells from the dataset to ensure that the technical noise do not affect the downstream analysis. We also remove the lowly expressed genes as they do not give much information and are unreliable for downstream statistical analysis (Bourgon et al., 2010). In order to account for the various sequencing depth of each cell, we normalized the raw counts using the deconvolution-based method (Lun et al., 2016a). We then identified the genes that have high variance in their biological component and use these genes for all downstream analysis. We then applied PCA and took the first 14 components of PCA as input to tSNE and used the first 2 components of tSNE to visualize our cells. The cells were then grouped into their putative clusters using the dynamic tree cut method. We used the *findMarkers* function from *Scran* package to identify the marker genes for each of the clusters (Lun et al., 2016b). *findMarkers* uses t-test for the statistical test and reports p-value of the high rank genes that are DE between the group and all other group. These marker genes were then used to manually annotate the cell types of a cluster (see

Supplementary file 3 for clustering annotation details). We also applied SingleR to define the cell types based on matched with annotated bulk datasets (Aran et al., 2019). We used the *plotDots* function from scater package to produce the dotplots (McCarthy et al., 2017).

Statistical analysis

Statistical analysis was carried out within Proteome Discoverer using an in-built Two-way ANOVA test with post-hoc Benjamini-Hochberg correction. Principal component analysis (PCA) and unsupervised hierarchical clustering based on a Euclidean distance-based complete-linkage matrix were performed using Rstudio (v. 1.2.5042, http://rstudio.com) with the ggplot2 package (v.3.3.2, https://ggplot2.tidyverse.org) that was also used to generate PCA plots and heat maps. For the integrated proteomic analysis, previously published young human glomerular and kidney tubulointerstitial data (PRIDE accession PXD022219) was re-processed with Proteome Discoverer to allow direct comparisons with newly acquired data. Then, kidney organoid, mouse and human proteomics datasets were compared using Spearman Rank correlation. Dataset comparisons, for both cellular and ECM cellular fractions, were performed separately for the matrisome proteins only and basement membrane proteins only. The ComplexHeatmap package (v2.2.0, (Gu et al., 2016); http://bioconductor.org/packages/release/bioc/html/ComplexHeatmap.html) was used to generate correlation plots.

ACKNOWLEDGMENTS

We acknowledge Faris Tengku who helped with the generation of wild-type iPSC, Joseph Luckman who helped to optimise immunofluorescence protocols, Karen Leigh Price and Maria Kolatsi-Joannou who helped with the human histology, and Anna-Li who helped with the description of the genetic variants using the ACMG criteria. The mass spectrometer and microscopes used in this study were purchased with grants from the Biotechnology and

Biological Sciences Research Council, Wellcome Trust and the University of Manchester Strategic Fund. Mass spectrometry was performed in the Biomolecular Analysis Core Facility, Faculty of Life Sciences, University of Manchester, and we thank David Knight, Ronan O'cualain and Stacey Warwood for advice and technical support and Julian Selley for bioinformatic support. The iPSC lines were generated at the Wellcome Trust Sanger Institute, under the Human Induced Pluripotent Stem Cell Initiative (HipSci) funded by a grant (WT098503) from the Wellcome Trust and Medical Research Council.

DECLARATION OF INTERESTS

The authors declare no conflicts of interests.

REFERENCES

Abrahamson, D.R., Isom, K., Roach, E., Stroganova, L., Zelenchuk, A., Miner, J.H., St John, P.L., 2007. Laminin compensation in collagen alpha3(IV) knockout (Alport) glomeruli contributes to permeability defects. J. Am. Soc. Nephrol. 18, 2465–2472. doi:10.1681/ASN.2007030328

Abrahamson, D.R., St John, P.L., 1993. Laminin distribution in developing glomerular basement membranes. Kidney Int. 43, 73–78. doi:10.1038/ki.1993.13

Abrahamson, D.R., St John, P.L., Stroganova, L., Zelenchuk, A., Steenhard, B.M., 2013. Laminin and type IV collagen isoform substitutions occur in temporally and spatially distinct patterns in developing kidney glomerular basement membranes. J. Histochem. Cytochem. 61, 706–718. doi:10.1369/0022155413501677

Aran, D., Looney, A.P., Liu, L., Wu, E., Fong, V., Hsu, A., Chak, S., Naikawadi, R.P., Wolters, P.J., Abate, A.R., Butte, A.J., Bhattacharya, M., 2019. Reference-based analysis of lung single-cell sequencing reveals a transitional profibrotic macrophage. Nat. Immunol. 20, 163–172. doi:10.1038/s41590-018-0276-y

Bantounas, I., Ranjzad, P., Tengku, F., Silajdžić, E., Forster, D., Asselin, M.-C., Lewis, P., Lennon, R., Plagge, A., Wang, Q., Woolf, A.S., Kimber, S.J., 2018. Generation of Functioning Nephrons by Implanting Human Pluripotent Stem Cell-Derived Kidney Progenitors. Stem Cell Rep. 10, 766–779. doi:10.1016/j.stemcr.2018.01.008

Barker, D.F., Hostikka, S.L., Zhou, J., Chow, L.T., Oliphant, A.R., Gerken, S.C., Gregory, M.C., Skolnick, M.H., Atkin, C.L., Tryggvason, K., 1990. Identification of mutations in the COL4A5 collagen gene in Alport syndrome. Science 248, 1224–1227. doi:10.1126/science.2349482

Bonnans, C., Chou, J., Werb, Z., 2014. Remodelling the extracellular matrix in development and disease. Nat. Rev. Mol. Cell Biol. 15, 786–801. doi:10.1038/nrm3904

Bourgon, R., Gentleman, R., Huber, W., 2010. Independent filtering increases detection power for high-throughput experiments. Proc. Natl. Acad. Sci. USA 107, 9546–9551. doi:10.1073/pnas.0914005107

Boutboul, S., Black, G.C.M., Moore, J.E., Sinton, J., Menasche, M., Munier, F.L., Laroche, L., Abitbol, M., Schorderet, D.F., 2006. A subset of patients with epithelial basement membrane corneal dystrophy have mutations in TGFBI/BIGH3. Hum. Mutat. 27, 553–557. doi:10.1002/humu.20331

Brown, K.L., Cummings, C.F., Vanacore, R.M., Hudson, B.G., 2017. Building collagen IV smart scaffolds on the outside of cells. Protein Sci. 26, 2151–2161. doi:10.1002/pro.3283

Byron, A., Randles, M.J., Humphries, J.D., Mironov, A., Hamidi, H., Harris, S., Mathieson, P.W., Saleem, M.A., Satchell, S.C., Zent, R., Humphries, M.J., Lennon, R., 2014. Glomerular cell cross-talk influences composition and assembly of extracellular matrix. J. Am. Soc. Nephrol. 25, 953–966. doi:10.1681/ASN.2013070795

Chew, C., Lennon, R., 2018. Basement membrane defects in genetic kidney diseases. Front. Pediatr. 6, 11. doi:10.3389/fped.2018.00011

Chiotaki, R., Petrou, P., Giakoumaki, E., Pavlakis, E., Sitaru, C., Chalepakis, G., 2007. Spatiotemporal distribution of Fras1/Frem proteins during mouse embryonic development. Gene Expr Patterns 7, 381–388. doi:10.1016/j.modgep.2006.12.001

Combes, A.N., Phipson, B., Lawlor, K.T., Dorison, A., Patrick, R., Zappia, L., Harvey, R.P., Oshlack, A., Little, M.H., 2019a. Single cell analysis of the developing mouse kidney provides deeper insight into marker gene expression and ligand-receptor crosstalk. Development 146. doi:10.1242/dev.178673

Combes, A.N., Zappia, L., Er, P.X., Oshlack, A., Little, M.H., 2019b. Single-cell analysis reveals congruence between kidney organoids and human fetal kidney. Genome Med. 11, 3. doi:10.1186/s13073-019-0615-0

Czerniecki, S.M., Cruz, N.M., Harder, J.L., Menon, R., Annis, J., Otto, E.A., Gulieva, R.E., Islas, L.V., Kim, Y.K., Tran, L.M., Martins, T.J., Pippin, J.W., Fu, H., Kretzler, M., Shankland, S.J., Himmelfarb, J., Moon, R.T., Paragas, N., Freedman, B.S., 2018. High-Throughput Screening Enhances Kidney Organoid Differentiation from Human Pluripotent Stem Cells and Enables Automated Multidimensional Phenotyping. Cell Stem Cell 22, 929–940.e4. doi:10.1016/j.stem.2018.04.022

Feitosa, N.M., Zhang, J., Carney, T.J., Metzger, M., Korzh, V., Bloch, W., Hammerschmidt, M., 2012. Hemicentin 2 and Fibulin 1 are required for epidermal-dermal junction formation and fin mesenchymal cell migration during zebrafish development. Dev. Biol. 369, 235–248. doi:10.1016/j.ydbio.2012.06.023

Forbes, T.A., Howden, S.E., Lawlor, K., Phipson, B., Maksimovic, J., Hale, L., Wilson, S., Quinlan, C., Ho, G., Holman, K., Bennetts, B., Crawford, J., Trnka, P., Oshlack, A., Patel, C., Mallett, A., Simons, C., Little, M.H., 2018. Patient-iPSC-Derived Kidney Organoids Show Functional Validation of a Ciliopathic Renal Phenotype and Reveal Underlying Pathogenetic Mechanisms. Am. J. Hum. Genet. 102, 816–831. doi:10.1016/j.ajhg.2018.03.014

Gatseva, A., Sin, Y.Y., Brezzo, G., Van Agtmael, T., 2019. Basement membrane collagens and disease mechanisms. Essays Biochem 63, 297–312. doi:10.1042/EBC20180071

Gu, Z., Eils, R., Schlesner, M., 2016. Complex heatmaps reveal patterns and correlations in multidimensional genomic data. Bioinformatics 32, 2847–2849. doi:10.1093/bioinformatics/btw313

Hale, L.J., Howden, S.E., Phipson, B., Lonsdale, A., Er, P.X., Ghobrial, I., Hosawi, S., Wilson, S., Lawlor, K.T., Khan, S., Oshlack, A., Quinlan, C., Lennon, R., Little, M.H., 2018. 3D organoid-derived human glomeruli for personalised podocyte disease modelling and drug screening. Nat. Commun. 9, 5167. doi:10.1038/s41467-018-07594-z

Hebert, J.D., Myers, S.A., Naba, A., Abbruzzese, G., Lamar, J.M., Carr, S.A., Hynes, R.O., 2020. Proteomic profiling of the ECM of xenograft breast cancer metastases in different organs reveals distinct metastatic niches. Cancer Res. 80, 1475–1485. doi:10.1158/0008-5472.CAN-19-2961

Howard, A.M., LaFever, K.S., Fenix, A.M., Scurrah, C.R., Lau, K.S., Burnette, D.T., Bhave, G., Ferrell, N., Page-McCaw, A., 2019. DSS-induced damage to basement membranes is repaired by matrix replacement and crosslinking. J. Cell Sci. 132. doi:10.1242/jcs.226860

Huang, D.W., Sherman, B.T., Lempicki, R.A., 2009. Systematic and integrative analysis of large gene lists using DAVID bioinformatics resources. Nat. Protoc. 4, 44–57. doi:10.1038/nprot.2008.211

Jassal, B., Matthews, L., Viteri, G., Gong, C., Lorente, P., Fabregat, A., Sidiropoulos, K., Cook, J., Gillespie, M., Haw, R., Loney, F., May, B., Milacic, M., Rothfels, K., Sevilla, C., Shamovsky, V., Shorser, S., Varusai, T., Weiser, J., Wu, G., Stein, L., Hermjakob, H., D'Eustachio, P., 2020. The Reactome Pathway Knowledgebase. Nucleic Acids Res. 48, D498–D503. doi:10.1093/nar/gkz1031

Jayadev, R., Chi, Q., Keeley, D.P., Hastie, E.L., Kelley, L.C., Sherwood, D.R., 2019. α-Integrins dictate distinct modes of type IV collagen recruitment to basement membranes. J. Cell Biol. 218, 3098–3116. doi:10.1083/jcb.201903124

Jayadev, R., Morais, M.R., Ellingford, J.M., Srinivasan, S., Naylor, R.W., Lawless, C., Li, A.S., Ingham, J.F., Hastie, E., Chi, Q., Fresquet, M., Koudis, N.-M., Thomas, H.B., O'Keefe, R.T., Williams, E., Adamson, A., Stuart, H.M., Banka, S., Smedley, D., Genomics England Research Consortium, Sherwood, D.R., Lennon, R., 2021. A basement membrane discovery pipeline uncovers network complexity, new regulators, and human disease associations. BioRxiv. doi:10.1101/2021.10.25.465762

Jayadev, R., Sherwood, D.R., 2017. Basement membranes. Curr. Biol. 27, R207–R211. doi:10.1016/j.cub.2017.02.006

Kashtan, C.E., Kim, Y., Lees, G.E., Thorner, P.S., Virtanen, I., Miner, J.H., 2001. Abnormal glomerular basement membrane laminins in murine, canine, and human Alport syndrome: aberrant laminin alpha2 deposition is species independent. J. Am. Soc. Nephrol. 12, 252–260. doi:10.1681/ASN.V122252

Keeley, D.P., Hastie, E., Jayadev, R., Kelley, L.C., Chi, Q., Payne, S.G., Jeger, J.L., Hoffman, B.D., Sherwood, D.R., 2020. Comprehensive Endogenous Tagging of Basement Membrane Components Reveals Dynamic Movement within the Matrix Scaffolding. Dev. Cell 54, 60–74.e7. doi:10.1016/j.devcel.2020.05.022

Kilpinen, H., Goncalves, A., Leha, A., Afzal, V., Alasoo, K., Ashford, S., Bala, S., Bensaddek, D., Casale, F.P., Culley, O.J., Danecek, P., Faulconbridge, A., Harrison, P.W., Kathuria, A., McCarthy, D., McCarthy, S.A., Meleckyte, R., Memari, Y., Moens, N., Soares, F., Mann, A., Streeter, I., Agu, C.A., Alderton, A., Nelson, R., Harper, S., Patel, M., White, A., Patel, S.R., Clarke, L., Halai, R., Kirton, C.M., Kolb-Kokocinski, A., Beales, P., Birney, E., Danovi, D., Lamond, A.I., Ouwehand, W.H., Vallier, L., Watt, F.M., Durbin, R., Stegle, O., Gaffney, D.J., 2017. Common genetic variation drives molecular heterogeneity in human iPSCs. Nature 546, 370–375. doi:10.1038/nature22403

Kruegel, J., Miosge, N., 2010. Basement membrane components are key players in specialized extracellular matrices. Cell Mol. Life Sci. 67, 2879–2895. doi:10.1007/s00018-010-0367-x

Kyprianou, C., Christodoulou, N., Hamilton, R.S., Nahaboo, W., Boomgaard, D.S., Amadei, G., Migeotte, I., Zernicka-Goetz, M., 2020. Basement membrane remodelling regulates mouse embryogenesis. Nature 582, 253–258. doi:10.1038/s41586-020-2264-2

Lennon, R., Byron, A., Humphries, J.D., Randles, M.J., Carisey, A., Murphy, S., Knight, D., Brenchley, P.E., Zent, R., Humphries, M.J., 2014. Global analysis reveals the complexity of the human glomerular extracellular matrix. J. Am. Soc. Nephrol. 25, 939–951. doi:10.1681/ASN.2013030233

Lenter, M., Uhlig, H., Hamann, A., Jenö, P., Imhof, B., Vestweber, D., 1993. A monoclonal antibody against an activation epitope on mouse integrin chain beta 1 blocks adhesion of lymphocytes to the endothelial integrin alpha 6 beta 1. Proc. Natl. Acad. Sci. USA 90, 9051–9055. doi:10.1073/pnas.90.19.9051

Li, S., Edgar, D., Fässler, R., Wadsworth, W., Yurchenco, P.D., 2003. The role of laminin in embryonic cell polarization and tissue organization. Dev. Cell 4, 613–624. doi:10.1016/s1534-5807(03)00128-x

Lipp, S.N., Jacobson, K.R., Hains, D.S., Schwarderer, A.L., Calve, S., 2021. 3D mapping reveals a complex and transient interstitial matrix during murine kidney development. J. Am. Soc. Nephrol. doi:10.1681/ASN.2020081204

Lun, A.T.L., Bach, K., Marioni, J.C., 2016a. Pooling across cells to normalize single-cell RNA sequencing data with many zero counts. Genome Biol. 17, 75. doi:10.1186/s13059-016-0947-7

Lun, A.T.L., McCarthy, D.J., Marioni, J.C., 2016b. A step-by-step workflow for low-level analysis of single-cell RNA-seq data with Bioconductor. [version 2; peer review: 3 approved, 2 approved with reservations]. F1000Res. 5, 2122. doi:10.12688/f1000research.9501.2

Maier, J.I., Rogg, M., Helmstädter, M., Sammarco, A., Schilling, O., Sabass, B., Miner, J.H., Dengjel, J., Walz, G., Werner, M., Huber, T.B., Schell, C., 2021. EPB41L5 controls podocyte extracellular matrix assembly by adhesome-dependent force transmission. Cell Rep. 34, 108883. doi:10.1016/j.celrep.2021.108883

Matsubayashi, Y., Louani, A., Dragu, A., Sánchez-Sánchez, B.J., Serna-Morales, E., Yolland, L., Gyoergy, A., Vizcay, G., Fleck, R.A., Heddleston, J.M., Chew, T.-L., Siekhaus, D.E., Stramer, B.M., 2017. A moving source of matrix components is essential for de novo basement membrane formation. Curr. Biol. 27, 3526–3534.e4. doi:10.1016/j.cub.2017.10.001

Matsubayashi, Y., Sánchez-Sánchez, B.J., Marcotti, S., Serna-Morales, E., Dragu, A., Díaz-de-la-Loza, M.-D.-C., Vizcay-Barrena, G., Fleck, R.A., Stramer, B.M., 2020. Rapid Homeostatic Turnover of Embryonic ECM during Tissue Morphogenesis. Dev. Cell 54, 33–42.e9. doi:10.1016/j.devcel.2020.06.005

McCarthy, D.J., Campbell, K.R., Lun, A.T.L., Wills, Q.F., 2017. Scater: pre-processing, quality control, normalization and visualization of single-cell RNA-seq data in R. Bioinformatics 33, 1179–1186. doi:10.1093/bioinformatics/btw777

Miner, J.H., 1999. Renal basement membrane components. Kidney Int. 56, 2016–2024. doi:10.1046/j.1523-1755.1999.00785.x

Miner, J.H., Sanes, J.R., 1996. Molecular and functional defects in kidneys of mice lacking collagen alpha 3(IV): implications for Alport syndrome. J. Cell Biol. 135, 1403–1413. doi:10.1083/jcb.135.5.1403

Miner, J.H., Yurchenco, P.D., 2004. Laminin functions in tissue morphogenesis. Annu. Rev. Cell Dev. Biol. 20, 255–284. doi:10.1146/annurev.cellbio.20.010403.094555

Morello, R., Zhou, G., Dreyer, S.D., Harvey, S.J., Ninomiya, Y., Thorner, P.S., Miner, J.H., Cole, W., Winterpacht, A., Zabel, B., Oberg, K.C., Lee, B., 2001. Regulation of glomerular basement membrane collagen expression by LMX1B contributes to renal disease in nail patella syndrome. Nat. Genet. 27, 205–208. doi:10.1038/84853

Morrissey, M.A., Keeley, D.P., Hagedorn, E.J., McClatchey, S.T.H., Chi, Q., Hall, D.H., Sherwood, D.R., 2014. B-LINK: a hemicentin, plakin, and integrin-dependent adhesion system that links tissues by connecting adjacent basement membranes. Dev. Cell 31, 319–331. doi:10.1016/j.devcel.2014.08.024

Naba, A., Clauser, K.R., Ding, H., Whittaker, C.A., Carr, S.A., Hynes, R.O., 2016. The extracellular matrix: Tools and insights for the “omics” era. Matrix Biol 49, 10–24. doi:10.1016/j.matbio.2015.06.003

Naba, A., Pearce, O.M.T., Del Rosario, A., Ma, D., Ding, H., Rajeeve, V., Cutillas, P.R., Balkwill, F.R., Hynes, R.O., 2017. Characterization of the extracellular matrix of normal and diseased tissues using proteomics. J. Proteome Res. 16, 3083–3091. doi:10.1021/acs.jproteome.7b00191

Naylor, R.W., Morais, M., Lennon, R., 2020. Complexities of the glomerular basement membrane. Nat. Rev. Nephrol. 17, 112–127. doi:10.1038/s41581-020-0329-y

Perez-Riverol, Y., Csordas, A., Bai, J., Bernal-Llinares, M., Hewapathirana, S., Kundu, D.J., Inuganti, A., Griss, J., Mayer, G., Eisenacher, M., Pérez, E., Uszkoreit, J., Pfeuffer, J., Sachsenberg, T., Yilmaz, S., Tiwary, S., Cox, J., Audain, E., Walzer, M., Jarnuczak, A.F., Ternent, T., Brazma, A., Vizcaíno, J.A., 2019. The PRIDE database and related tools and resources in 2019: improving support for quantification data. Nucleic Acids Res. 47, D442–D450. doi:10.1093/nar/gky1106

Petrou, P., Makrygiannis, A.K., Chalepakis, G., 2008. The Fras1/Frem family of extracellular matrix proteins: structure, function, and association with Fraser syndrome and the mouse bleb phenotype. Connect Tissue Res 49, 277–282. doi:10.1080/03008200802148025

Randles, M.J., Humphries, M.J., Lennon, R., 2017. Proteomic definitions of basement membrane composition in health and disease. Matrix Biol 57–58, 12–28. doi:10.1016/j.matbio.2016.08.006

Randles, M.J., Woolf, A.S., Huang, J.L., Byron, A., Humphries, J.D., Price, K.L., Kolatsi-Joannou, M., Collinson, S., Denny, T., Knight, D., Mironov, A., Starborg, T., Korstanje, R., Humphries, M.J., Long, D.A., Lennon, R., 2015. Genetic background is a key determinant of glomerular extracellular matrix composition and organization. J. Am. Soc. Nephrol. 26, 3021–3034. doi:10.1681/ASN.2014040419

Romero-Guevara, R., Ioannides, A., Xinaris, C., 2020. Kidney organoids as disease models: strengths, weaknesses and perspectives. Front. Physiol. 11, 563981. doi:10.3389/fphys.2020.563981

Rooney, K.M., Woolf, A.S., Kimber, S.J., 2021. Towards Modelling Genetic Kidney Diseases with Human Pluripotent Stem Cells. Nephron 145, 285–296. doi:10.1159/000514018

Sasaki, T., Fässler, R., Hohenester, E., 2004. Laminin: the crux of basement membrane assembly. J. Cell Biol. 164, 959–963. doi:10.1083/jcb.200401058

Shannon, P., Markiel, A., Ozier, O., Baliga, N.S., Wang, J.T., Ramage, D., Amin, N., Schwikowski, B., Ideker, T., 2003. Cytoscape: a software environment for integrated models of biomolecular interaction networks. Genome Res. 13, 2498–2504. doi:10.1101/gr.1239303

Szklarczyk, D., Franceschini, A., Wyder, S., Forslund, K., Heller, D., Huerta-Cepas, J., Simonovic, M., Roth, A., Santos, A., Tsafou, K.P., Kuhn, M., Bork, P., Jensen, L.J., von Mering, C., 2015. STRING v10: protein-protein interaction networks, integrated over the tree of life. Nucleic Acids Res. 43, D447-52. doi:10.1093/nar/gku1003

Takasato, M., Er, P.X., Chiu, H.S., Maier, B., Baillie, G.J., Ferguson, C., Parton, R.G., Wolvetang, E.J., Roost, M.S., Chuva de Sousa Lopes, S.M., Little, M.H., 2015. Kidney organoids from human iPS cells contain multiple lineages and model human nephrogenesis. Nature 526, 564–568. doi:10.1038/nature15695

Tanigawa, S., Islam, M., Sharmin, S., Naganuma, H., Yoshimura, Y., Haque, F., Era, T., Nakazato, H., Nakanishi, K., Sakuma, T., Yamamoto, T., Kurihara, H., Taguchi, A., Nishinakamura, R., 2018. Organoids from Nephrotic Disease-Derived iPSCs Identify Impaired NEPHRIN Localization and Slit Diaphragm Formation in Kidney Podocytes. Stem Cell Rep. 11, 727–740. doi:10.1016/j.stemcr.2018.08.003

Tian, P., Lennon, R., 2019. The myriad possibility of kidney organoids. Curr Opin Nephrol Hypertens 28, 211–218. doi:10.1097/MNH.0000000000000498

Urbano, J.M., Torgler, C.N., Molnar, C., Tepass, U., López-Varea, A., Brown, N.H., de Celis, J.F., Martín-Bermudo, M.D., 2009. Drosophila laminins act as key regulators of basement membrane assembly and morphogenesis. Development 136, 4165–4176. doi:10.1242/dev.044263

Wood, K.A., Rowlands, C.F., Thomas, H.B., Woods, S., O'Flaherty, J., Douzgou, S., Kimber, S.J., Newman, W.G., O'Keefe, R.T., 2020. Modelling the developmental spliceosomal craniofacial disorder Burn-McKeown syndrome using induced pluripotent stem cells. PLoS One 15, e0233582. doi:10.1371/journal.pone.0233582

Wu, H., Uchimura, K., Donnelly, E.L., Kirita, Y., Morris, S.A., Humphreys, B.D., 2018. Comparative Analysis and Refinement of Human PSC-Derived Kidney Organoid Differentiation with Single-Cell Transcriptomics. Cell Stem Cell 23, 869–881.e8. doi:10.1016/j.stem.2018.10.010

Yamamura, T., Horinouchi, T., Adachi, T., Terakawa, M., Takaoka, Y., Omachi, K., Takasato, M., Takaishi, K., Shoji, T., Onishi, Y., Kanazawa, Y., Koizumi, M., Tomono, Y., Sugano, A., Shono, A., Minamikawa, S., Nagano, C., Sakakibara, N., Ishiko, S., Aoto, Y., Kamura, M., Harita, Y., Miura, K., Kanda, S., Morisada, N., Rossanti, R., Ye, M.J., Nozu, Y., Matsuo, M., Kai, H., Iijima, K., Nozu, K., 2020a. Development of an exon skipping therapy for X-linked Alport syndrome with truncating variants in COL4A5. Nat. Commun. 11, 2777. doi:10.1038/s41467-020-16605-x

Yamamura, T., Horinouchi, T., Nagano, C., Omori, T., Sakakibara, N., Aoto, Y., Ishiko, S., Nakanishi, K., Shima, Y., Nagase, H., Takeda, H., Rossanti, R., Ye, M.J., Nozu, Y., Ishimori, S., Ninchoji, T., Kaito, H., Morisada, N., Iijima, K., Nozu, K., 2020b. Genotype-phenotype correlations influence the response to angiotensin-targeting drugs in Japanese patients with male X-linked Alport syndrome. Kidney Int. 98, 1605–1614. doi:10.1016/j.kint.2020.06.038

Young, M.D., Mitchell, T.J., Vieira Braga, F.A., Tran, M.G.B., Stewart, B.J., Ferdinand, J.R., Collord, G., Botting, R.A., Popescu, D.-M., Loudon, K.W., Vento-Tormo, R., Stephenson, E., Cagan, A., Farndon, S.J., Del Castillo Velasco-Herrera, M., Guzzo, C., Richoz, N., Mamanova, L., Aho, T., Armitage, J.N., Riddick, A.C.P., Mushtaq, I., Farrell, S., Rampling, D., Nicholson, J., Filby, A., Burge, J., Lisgo, S., Maxwell, P.H., Lindsay, S., Warren, A.Y., Stewart, G.D., Sebire, N., Coleman, N., Haniffa, M., Teichmann, S.A., Clatworthy, M., Behjati, S., 2018. Single-cell transcriptomes from human kidneys reveal the cellular identity of renal tumors. Science 361, 594–599. doi:10.1126/science.aat1699

Zenker, M., Aigner, T., Wendler, O., Tralau, T., Müntefering, H., Fenski, R., Pitz, S., Schumacher, V., Royer-Pokora, B., Wühl, E., Cochat, P., Bouvier, R., Kraus, C., Mark, K., Madlon, H., Dötsch, J., Rascher, W., Maruniak-Chudek, I., Lennert, T., Neumann, L.M., Reis, A., 2004. Human laminin beta2 deficiency causes congenital nephrosis with mesangial sclerosis and distinct eye abnormalities. Hum. Mol. Genet. 13, 2625–2632. doi:10.1093/hmg/ddh284

FIGURE LEGENDS

Figure 1. **Kidney organoid basement membranes are altered in human disease**. (A) Schematic representing the differentiation of iPSC's to 3D kidney organoids. (B) Whole-mount immunofluorescence for kidney cell types: left image shows glomerular structures (g) with WT1$^+$ cells and CDH1$^+$ tubule segments (dashed line); right image shows a glomerular-like structure (g) containing podocytes (NPHS1$^+$) and endothelial cells (CD31$^+$). (C) Representative photomicrographs of day 18 kidney organoids (left) and human and mouse fetal kidneys (right) to demonstrate the comparable histological structure; inset shows an organoid glomerular structure (g). (D) Transmission electron photomicrographs of a glomerular- (upper panels) and tubule-like structures (lower panels) in a day 25 kidney organoid. In the top-right zoomed area, note features of organoid podocytes (P): a primary process (PP) and distinct intercalating foot processes (thin arrowheads) lining a basement membrane (arrows). Asterisks indicate glycogen granules. In the lower panels, a tubule-like structure in the organoid, and a basement membrane (arrows) labelled with a 10-nm gold-conjugated anti-laminin antibody (see large arrowheads in the zoomed area). (E) Right,

pedigree from a family with a pathogenic missense variant in *COL4A5* (c.3695G>A; p.Gly1232Asp, posterior probability 0.988) and a uncertain significance variant in *COL4A4* (c.3286C>T; p.Pro1096Ser [VUS], posterior probability 0.5). Left, Sanger sequencing data for the *COL4A5* variant found in the mother and 2 siblings, which changes the amino acid from glycine to aspartic acid located in the triple-helical region of the collagen IV trimer. (F) Representative whole mount immunofluorescence images of wild-type and Alport kidney organoids show glomerular structures (g) containing $WT1^+$ cells, and an intricate cluster of $CDH1^+$ epithelial tubules. (G) Immunofluorescence for LAMB2 shows increased protein deposition in extraglomerular sites (*). NPHS2 was used as a podocyte marker to identify glomerular structures (g). (H) Immunoblotting for LAMB2 using total lysates from wild-type (*n*=3) and Alport organoids (*n*=3 per group): bar chart shows relative fold change (to wild-type). LAMB2 band optical density was normalized by Ponceau stain and compared by one-way ANOVA and Tukey's multiple comparison tests (**p*-value < 0.05; ns: not significant). Pooled data are presented as median, error bars indicate the 95% confidence interval for the median. See Figure 1-Data source 1. See Figure 1-figures supplement 1-3.

Figure 2. **Sequential assembly of basement membranes components**. (A) Confocal immunofluorescence microscopy of wild-type kidney organoids showing the temporal emergence and BM co-distribution of COL4A1 and panlaminin and (B) perlecan and nidogen on days 11, 18 and 25 of differentiation. NPHS1 and CD31 were used respectively as markers for podocyte and endothelial cells in glomerular like structures (g). Arrowheads indicate interrupted BM segments, large arrows indicate diffuse BM networks, and thin arrows indicate intracellular droplets of BM proteins.

Figure 3. **Time course proteomics reveals complex dynamics of basement membrane assembly**. (A) Schematic for sample enrichment for matrix (ECM) proteins for tandem MS analysis (created with BioRender.com). (B) Bar graphs show the relative abundance of matrix proteins and non-matrix proteins identified by MS analysis in the cellular and ECM

fractions of kidney organoids on days 14, 18 and 25 (*n*=3 pools per time point). Pooled data are presented as median, error bars indicate the 95% confidence interval for the median. (C) Venn diagrams showing identification overlap for matrix proteins detected in organoids on days 14, 18 and 25. (D) Matrix proteins are classified as basement membrane, other structural and ECM-associated proteins. Bar charts show the number of matrix proteins per each category in both cellular and ECM fractions, and line charts show the changes in the relative abundance (percentage of total matrix abundance) for the matrix categories over the time course differentiation. Pooled data are presented as median, error bars indicate the 95% confidence interval for the median. (E) Protein interaction network showing all BM proteins identified over the kidney organoid time course MS study (nodes represent proteins and connecting lines indicate protein-protein interaction). (F) Heat map showing the $\log_{10}$-transformed abundance levels of BM proteins identified in the ECM fraction along kidney organoid differentiation time course (proteins detected only in one time-point are not shown). (G) Volcano plots show the $\log_2$-fold change (x-axis) versus $-\log_{10}$-*p*-value (y-axis) for proteins differentially expressed in the ECM fraction of kidney organoids from day 14 to 18, and 18 to 25 (*n*=3 per time point). Key BM proteins significantly up-regulated (FC $\geq$ 1.5, *p*-value < 0.05, Two-way ANOVA test, *n*=3) are indicated. (H) Time-dependant changes in the relative abundance (percentage of total protein intensity) of key BM proteins in the ECM fraction of kidney organoids during differentiation. Pooled data are presented as median. See Figure 3-figure supplement 1.

Figure 4. **Key collagen IV and laminin isoform transitions occur during kidney organoid differentiation**. (A) Immunofluorescence for key collagen IV and laminin isoforms showing their emergence and distribution in kidney organoid BM. Panlaminin antibody was used to co-label organoid BM; glomerular structures are indicated (g). (B) Re-analysis of a kidney organoid scRNA-seq dataset GSE114802, (Combes et al., 2019b) confirms cellular specificity for collagen IV and laminin isoform gene expression. tSNE plots represent the cell type clusters identified, and colour intensity indicate the cell-specific level of expression for

the selected BM genes. (C) Proteomic analysis of laser-captured maturing glomeruli from E19 mouse kidneys (*n*=4). Histological images show the laser dissected glomeruli, and the protein interaction network shows 25 BM proteins identified (nodes represent proteins and connecting lines indicate protein-protein interaction). (D) Immunofluorescence for specific collagen IV isoforms in maturing glomeruli in E19 mouse kidney and in glomerular structures (indicated by dashed lines) in day 25 organoids. NPHS2 was used to label podocytes. Arrowheads indicate outer Bowman's capsule (mouse) or glomerular surface (organoid), large arrows indicate GBM (mouse) or GBM-like deposition (organoid); thin arrows indicate mesangial matrix (mouse) or internal glomerular deposition (organoid). See Figure 4-figure supplement 1.

Figure 5. **Basement membranes in mouse fetal kidneys are comparable to kidney organoids**. (A) Schematic representation of the E19 mouse kidney sampled for MS-based proteomics, and a Venn diagram showing the overlap for matrix proteins identified in the cellular and ECM fractions. (B) Bar charts show enrichment for matrix proteins in both cellular and ECM fractions (*n*=6), as indicated by the number and relative abundance of proteins in each matrix category. Pooled data are presented as median, error bars indicate the 95% confidence interval for the median. (C) Expanded fetal mouse kidney matrisome represented as a protein interaction network (nodes represent proteins identified in this and in a previous study (Lipp et al., 2021), and connecting lines indicate protein-protein interaction). (D) Comparison of BM proteins identified in the E19 mouse fetal kidney* (MFK) and human kidney organoids (HKO) during differentiation (asterisks indicate that corresponding human ortholog proteins are shown). (E) Spearman rank correlation analysis for matrix and BM protein abundance (ECM fraction) comparisons between E19 mouse fetal kidney (MFK) and human kidney organoids (HKO). (F) Re-analysis of a E18.5 mouse kidney scRNA-seq dataset GSE108291, (Combes et al., 2019a) confirms cellular specificity for collagen IV and laminin isoform gene expression. tSNE plots represent the cell type clusters

identified, and colour intensity indicate the cell-specific level of expression for the selected BM genes. See Figures 5-figures supplement 1 and 2.

Figure 6. **Basement membranes are dynamic through embryonic development to adulthood**. (A) Integrative interactome showing a common core of 44 BM proteins across day 25 organoid, E19 mouse kidney, adult human glomerular and tubulointerstitial compartments. Venn diagrams indicate in which dataset each BM protein was detected. Nodes represent proteins, and lines indicate protein-protein interactions. (B) Spearman rank correlation analysis for matrix and BM protein abundance (ECM fraction) comparisons between E19 mouse fetal kidney (MFK), human kidney organoids (HKO) and adult human glomerulus and kidney tubulointerstitium. (C) Re-analysis of an adult human kidney scRNA-seq dataset EGAS00001002553, (Young et al., 2018)) confirms cellular specificity for collagen IV and laminin isoform gene expression. tSNE plots represent the cell type clusters identified, and colour intensity indicate the cell-specific level of expression for the selected BM genes (*proximal tubule cells were not included). (D) Cell expression of minor BM components through kidney development to adulthood. Dot plots show the level of expression of target genes in all published datasets re-analysed in this study (*proximal tubule cells were not included). See Figure 6-figure supplement 1.

Figure 7. Overview of the developmental milestones in human and mouse kidney morphogenesis, and a comparison human kidney organoids. Differentiation is dated in human as week-post conception (**wpc**), in mouse as embryonic days (**E**) and in kidney organoids as **day** of differentiation, and measures (cm or mm) indicate specimen size in each model. Three sets of embryonic kidneys develop in mammals in a temporal sequence: from the pronephros to the mesonephros (both temporary), and then to the metanephros (permanent). Metanephric nephron formation (nephrogenesis) commences in humans at 5 wpc, in mice at E10.5, and in kidney organoid from day 11, when the laminin starts to deposit as basement membrane networks. Following the same developmental stage in

human and mouse kidneys, kidney organoids start to form discernable renal vesicles on day 14, and distinct comma- and S-shaped bodies on day 18; day 25 organoids, which most closely resemble late capillary loop stage nephrons *in vivo*, comprise more mature structures including glomeruli with capillary lumens, proximal tubules, and distal tubules. Meanwhile a conserved sequence of basement membrane assembly was detected in kidney organoids, and laminin and collagen IV developmental isoform transitions were identified between day 14 and day 25.

SUPPLEMENTARY FIGURES AND FILES

Figure 1–figure supplement 1. Morphological characteristics of wild-type kidney organoids and fetal human kidney. (A) Bright field images (left) and H&E staining (right) of human kidney organoids on day 11, 14, 18 and 25 of differentiation. (B) H&E staining of human fetal kidney at 8 wpc, 12 wpc, 17 wpc, and 21 wpc highlights normal human kidney development. (C) Immunofluorescence for integrin beta-1 (ITGB1) in day 25 kidney organoid (wild-type). Anti-panlaminin or anti-collagen IV antibodies were used to label basement membranes. In the glomerulus (g), note the distribution of ITGB1 adjacent to the basement membrane.

Figure 1-figure supplement 2. Ultrastructure of glomerular-like structures in day 25 human kidney organoids. (A) Transmission electron microscopy of day 25 kidney organoids shows advanced differentiation of glomerular structures. In the zoomed areas (1 and 2) note podocytes (P) displaying long branching primary processes (PP) and a layer of intercalated foot processes (thin arrow) lining a distinct basement membrane (thin arrows). Asterisks indicate accumulation of glycogen granules, and large arrowheads tight cell junctions between maturing podocyte processes. In the lower panels, note in the zoomed area (3) a deposition of basement membrane-like matrix between podocyte processes within a glomerular structure. (B) Note the presence of likely endothelial cells (E) and podocytes (P). In the zoomed area, note a layer of podocyte foot processes (arrowheads) and an

endothelial cell (E), but deposition of matrix- and BM-like electron-dense material in between (asterisks).

Figure 1–figure supplement 3. Differentiation of wild-type and Alport kidney organoids. Whole-mount immunofluorescence of wild-type and Alport kidney organoids shows comparable deposition of COL4A4 in BM-like structures (arrows) within NPHS1+/CD31+ glomerular-like structures (g).

Figure 3–figure supplement 1. Time course proteomic analysis of kidney organoid differentiation. (A) Gene ontology (GO) term enrichment analysis for cellular component annotations associated with proteins detected in the cellular and ECM fractions of kidney organoids by mass spectrometry (MS). GO terms were considered enriched when False Discovery Rate (FDR) < 0.10. (B) Protein interaction network depicts matrisome proteins identified in kidney organoids by MS over the differentiation time course (nodes represent proteins and connecting lines indicate a reported protein-protein interaction). (C) Principal component analysis (PCA) for the matrix proteins identified by MS in the cellular (left plot) and ECM (right plot) fractions of kidney organoids. (D) Top 15 most abundant BM proteins found in kidney organoids by MS. Proteins were ranked according to their normalized abundance levels (LFQ-intensities). Pooled data are shown as median, error bars indicate the 95% confidence interval for the median. (E) Volcano plots show the log2-fold change (x-axis) vs. -log10-p-value (y-axis) for proteins differentially expressed in the cellular fraction of kidney organoids from day 14 to 18, and 18 to 25. Key BM proteins significantly up-regulated (FC>1.5, *p*-value < 0.05, Two-way ANOVA test, *n*=3) are indicated (F) Pathway enrichment analysis for proteins differentially expressed during kidney organoid differentiation: bar charts depict log-transformed FDR for the top-most enriched pathways (FDR<0.10). Pathway terms shown were simplified.

Figure 4–figure supplement 1. Single cell-RNA sequencing data analysis of human kidney organoids. (A) Dotplot depicting the cell-specific level of expression of 160 BM gene collection in 25 days kidney organoids. (B) tSNE plot indicates gene expression of LIMX1b and EPB41L5 in day 25 kidney organoids. Arrows indicate podocyte clusters. Data shown in (A) and (B) were obtained from a re-analysis of a publicly available scRNA-seq dataset GSE114802; (Combes et al., 2019b). (C) Bar charts show the time-dependent changes in protein abundance of EPB41L5 in kidney organoids (*n*=3 per time point). Pooled data are shown as median, error bars indicate the 95% confidence interval for the median. Two-way ANOVA test: **p*-value <0.05.

Figure 5–figure supplement 1. Proteomic analysis of E19 mouse fetal kidney and correlational comparison with kidney organoid proteomics. (A) Gene ontology (GO) term enrichment analysis for cellular component annotations associated with proteins detected by MS in the cellular and ECM. (B) GO biological process annotations enriched for top 100 most abundant proteins detected by MS in the cellular and ECM. (C) Top 20 most abundant BM proteins found in the E19 mouse kidney by MS. Proteins were ranked according to their normalized abundance levels (LFQ-intensities). Pooled data are presented as median, error bars indicate the 95% confidence interval for the median. (D) Comparison of other structural matrix and ECM-associated proteins identified in the E19 mouse kidney and kidney organoids over differentiation. (E) Spearman rank correlation plots depicting the r coefficient values for matrix and BM protein abundance (ECM fraction) comparisons between the E19 mouse kidney and kidney organoids.

Figure 5–figure supplement 2. Single-cell RNA sequencing analysis of human fetal kidney. Re-analysis of 8/9-wpc human kidney scRNA-seq datasets (EGAS00001002325, EGAS00001002553; Young et al., 2018) confirms cellular specificity for collagen IV and laminin isoform gene expression. tSNE plots represent the cell type clusters identified, and colour intensity indicates the cell-specific level of expression for the selected BM genes.

Figure 6–figure supplement 1. Integrated correlational analysis of organoid and *in vivo* kidney datasets. Spearman rank correlation plots depicting the r coefficient values for matrix and BM protein abundance (ECM fraction) between E19 mouse kidney, kidney organoids and adult human kidney proteomic datasets.

Supplementary file 1. Human fetal kidney and hiPSC general information.

Supplementary file 2. Human kidney organoid proteome and matrix proteins

Supplementary file 3. scRNA-seq kidney datasets- cell clustering and expression data.

Supplementary file 4. E19 mouse maturing glomerulus proteome and matrix proteins.

Supplementary file 5. E19 mouse kidney proteome and matrix proteins.

Supplementary file 6. Human adult kidney glomerular and tubulointerstitial proteome and matrix proteins.

SOURCE DATA

This project contains the following source data hosted at: https://doi.org/10.6084/m9.figshare.c.5429628

Figure 1 Original IF Images: **B** Whole-mount immunofluorescence for kidney cell types; **F** Representative whole mount immunofluorescence images of wild-type and Alport kidney organoids; **G** Immunofluorescence for LAMB2.

Figure 1 Original light microscope Images: **C** Representative photomicrographs of day 18 kidney organoids (left) and human and mouse fetal kidneys (right).

Figure 1 Original TEM Images: **D** Transmission electron micrographs of tubular BM in day 25 kidney organoid and E19 mouse fetal kidney.

Figure 1 Original western blotting image: **H** Immunoblotting for LAMB2 using total lysates from wild-type and Alport organoids.

Figure 2 Original IF Images: **A** Confocal immunofluorescence microscopy of wild-type kidney organoids; **B** perlecan and nidogen on days 11, 18 and 25 of differentiation.

Figure 4 Original IF Images: **A** Immunofluorescence for key type IV collagen and laminin isoforms showing their emergence and distribution in kidney organoid BM; **D** Immunofluorescence for specific collagen IV isoforms in maturing glomeruli in E19 mouse kidney and in glomerular structures (indicated by dashed lines) in day 25 organoids.

Figure 1-figure supplement 2A Original TEM photomicrographs: **A** Transmission electron microscopy of day 25 kidney organoids shows advanced differentiation of glomerular structures.

Figure 1-figure supplement 2B Original TEM photomicrographs: **B** Transmission electron microscopy of day 25 kidney organoids shows advanced differentiation of glomerular structures.

Figure 1-figure supplement 1C Original IF images: **C** Immunofluorescence for integrin beta-1 (ITGB1) in day 25 kidney organoid (wild-type). Anti-panlaminin or anti-collagen IV antibodies were used to label basement membranes.

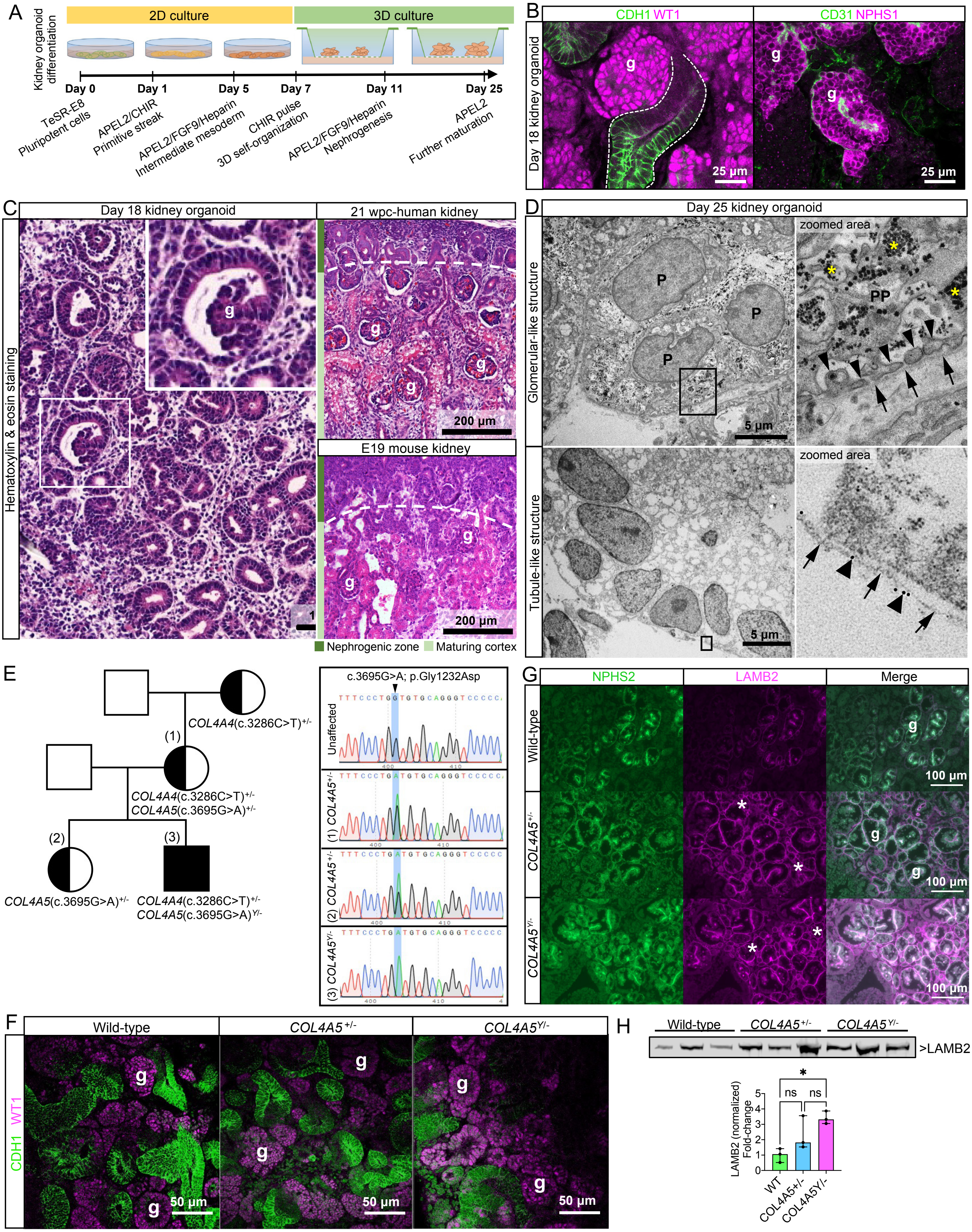
A
Kidney organoid differentiation
2D culture
3D culture
Day 0
Day 1
Day 5
Day 7
Day 11
Day 25
TeSR-E8
Pluripotent cells
APEL2/CHIR
Primitive streak
APEL2/FGF9/Heparin
Intermediate mesoderm
CHIR pulse
3D self-organization
APEL2/FGF9/Heparin
Nephrogenesis
APEL2
Further maturation
B
Day 18 kidney organoid
CDH1 WT1
CD31 NPHS1
g
g
g
25 µm
25 µm
C
Hematoxylin & eosin staining
Day 18 kidney organoid
21 wpc-human kidney
E19 mouse kidney
g
g
g
g
g
g
g
200 µm
200 µm
Nephrogenic zone
Maturing cortex
D
Day 25 kidney organoid
Glomerular-like structure
Tubule-like structure
zoomed area
zoomed area
P
P
P
PP
*
5 µm
5 µm
E
COL4A4(c.3286C>T)+/-
(1)
COL4A4(c.3286C>T)+/-
COL4A5(c.3695G>A)+/-
(2)
(3)
COL4A5(c.3695G>A)+/-
COL4A4(c.3286C>T)+/-
COL4A5(c.3695G>A)Y/-
c.3695G>A; p.Gly1232Asp
Unaffected
(1) COL4A5+/-
(2) COL4A5+/-
(3) COL4A5Y/-
TTTCCCTGGTGTGCAGGGTCCCCC
TTTCCCTGATGTGCAGGGTCCCCC
400
410
F
Wild-type
COL4A5+/-
COL4A5Y/-
CDH1 WT1
g
50 µm
50 µm
50 µm
G
NPHS2
LAMB2
Merge
Wild-type
COL4A5+/-
COL4A5Y/-
g
*
100 µm
100 µm
100 µm
H
Wild-type
COL4A5+/-
COL4A5Y/-
>LAMB2
LAMB2 (normalized) Fold-change
0
1
2
3
4
5
*
ns
ns
WT
COL4A5+/-
COL4A5Y/-

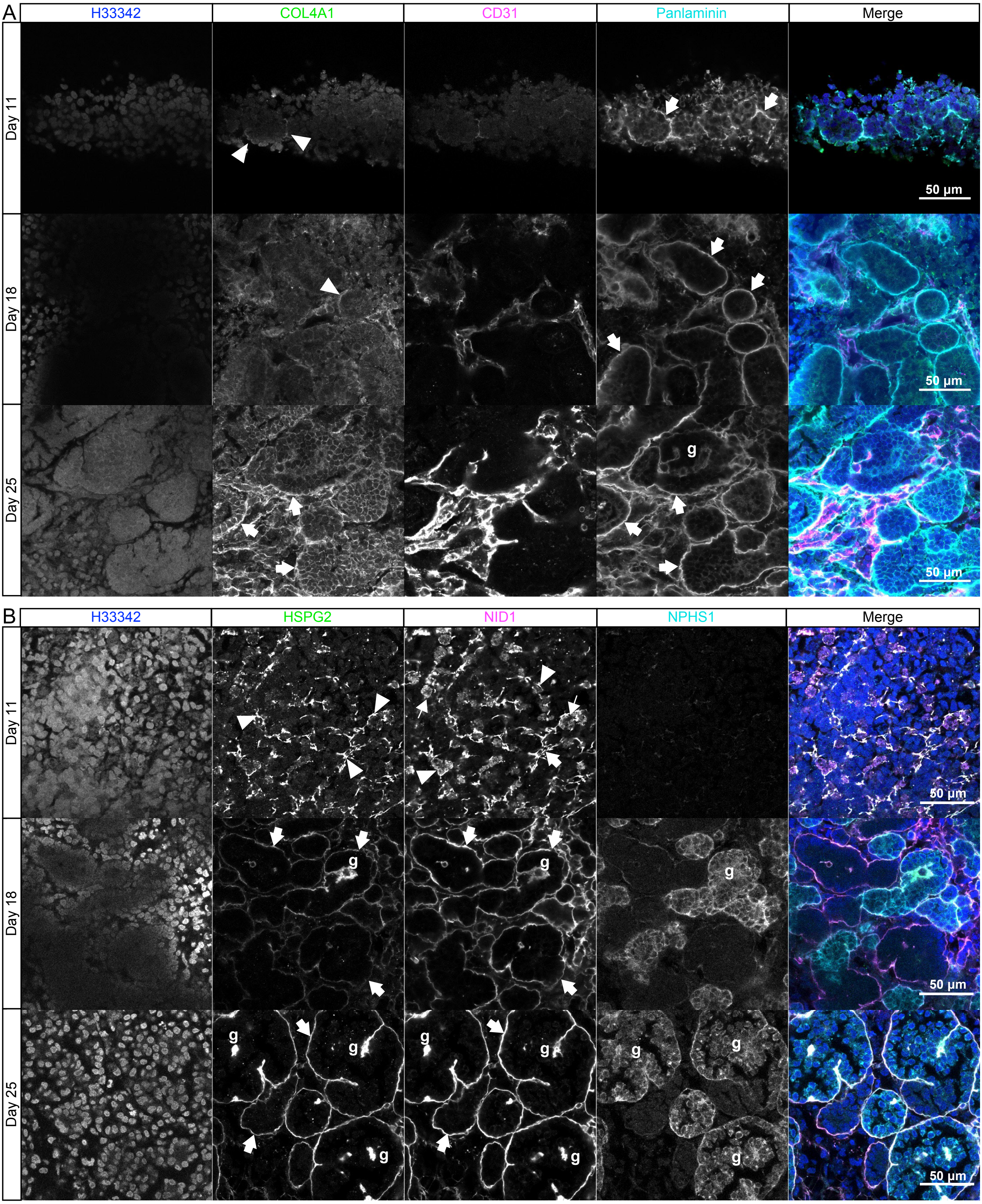
A
H33342
COL4A1
CD31
Panlaminin
Merge
Day 11
Day 18
Day 25
50 µm
50 µm
50 µm
g
B
H33342
HSPG2
NID1
NPHS1
Merge
Day 11
Day 18
Day 25
g
50 µm
50 µm
50 µm

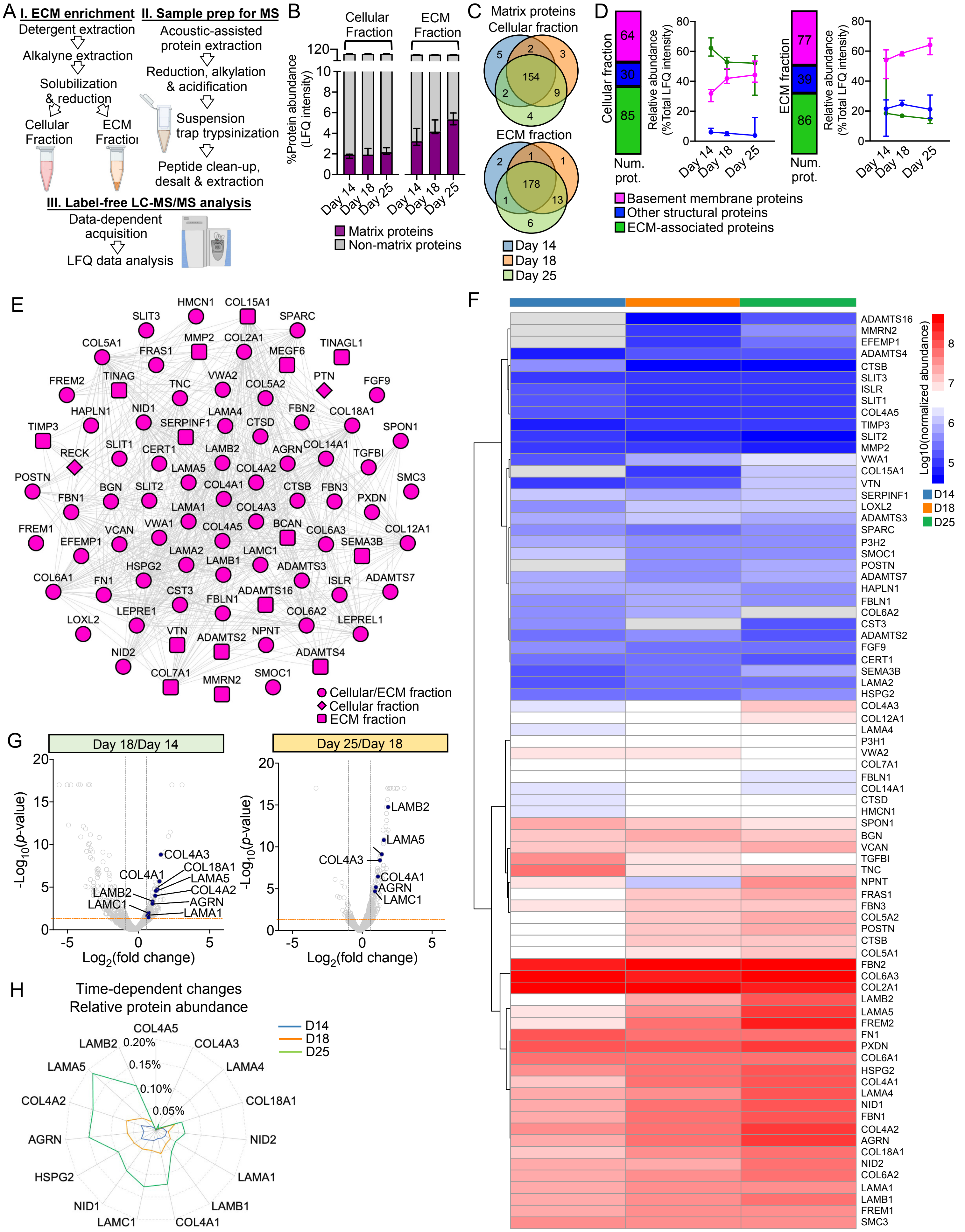
A
I. ECM enrichment
Detergent extraction
Alkalyne extraction
Solubilization & reduction
Cellular Fraction
ECM Fraction
II. Sample prep for MS
Acoustic-assisted protein extraction
Reduction, alkylation & acidification
Suspension trap trypsinization
Peptide clean-up, desalt & extraction
III. Label-free LC-MS/MS analysis
Data-dependent acquisition
LFQ data analysis
B
Cellular Fraction
ECM Fraction
%Protein abundance (LFQ intensity)
120
10
8
6
4
2
0
Day 14
Day 18
Day 25
Matrix proteins
Non-matrix proteins
C
Matrix proteins
Cellular fraction
5
2
3
154
2
9
4
ECM fraction
2
1
1
178
1
13
6
Day 14
Day 18
Day 25
D
Cellular fraction
64
30
85
Num. prot.
Relative abundance (%Total LFQ intensity)
80
60
40
20
0
Day 14
Day 18
Day 25
ECM fraction
77
39
86
Num. prot.
Basement membrane proteins
Other structural proteins
ECM-associated proteins
E
HMCN1
COL15A1
SLIT3
SPARC
COL5A1
MMP2
COL2A1
FRAS1
MEGF6
TINAGL1
FREM2
TINAG
TNC
VWA2
COL5A2
PTN
FGF9
HAPLN1
NID1
LAMA4
FBN2
COL18A1
TIMP3
SERPINF1
CTSD
SPON1
RECK
SLIT1
CERT1
LAMB2
AGRN
COL14A1
TGFBI
LAMA5
COL4A2
POSTN
BGN
SLIT2
COL4A1
CTSB
FBN3
SMC3
FBN1
LAMA1
COL4A3
PXDN
VWA1
COL4A5
BCAN
COL6A3
COL12A1
FREM1
VCAN
EFEMP1
SEMA3B
LAMA2
LAMC1
HSPG2
LAMB1
ADAMTS3
COL6A1
FN1
ISLR
ADAMTS7
CST3
ADAMTS16
LEPRE1
FBLN1
COL6A2
LOXL2
LEPREL1
VTN
NPNT
ADAMTS2
NID2
ADAMTS4
COL7A1
MMRN2
SMOC1
Cellular/ECM fraction
Cellular fraction
ECM fraction
F
ADAMTS16
MMRN2
EFEMP1
ADAMTS4
CTSB
SLIT3
ISLR
SLIT1
COL4A5
TIMP3
SLIT2
MMP2
VWA1
COL15A1
VTN
SERPINF1
LOXL2
ADAMTS3
SPARC
P3H2
SMOC1
POSTN
ADAMTS7
HAPLN1
FBLN1
COL6A2
CST3
ADAMTS2
FGF9
CERT1
SEMA3B
LAMA2
HSPG2
COL4A3
COL12A1
LAMA4
P3H1
VWA2
COL7A1
FBLN1
COL14A1
CTSD
HMCN1
SPON1
BGN
VCAN
TGFBI
TNC
NPNT
FRAS1
FBN3
COL5A2
POSTN
CTSB
COL5A1
FBN2
COL6A3
COL2A1
LAMB2
LAMA5
FREM2
FN1
PXDN
COL6A1
HSPG2
COL4A1
LAMA4
NID1
FBN1
COL4A2
AGRN
COL18A1
NID2
COL6A2
LAMA1
LAMB1
FREM1
SMC3
Log10(normalized abundance)
8
7
6
5
D14
D18
D25
G
Day 18/Day 14
-Log10(p-value)
20
15
10
5
0
-5
0
5
Log2(fold change)
COL4A3
COL4A1
COL18A1
LAMA5
COL4A2
LAMB2
AGRN
LAMC1
LAMA1
Day 25/Day 18
LAMB2
LAMA5
COL4A3
COL4A1
AGRN
LAMC1
H
Time-dependent changes
Relative protein abundance
COL4A5
COL4A3
LAMA4
COL18A1
NID2
LAMA1
LAMB1
COL4A1
LAMC1
NID1
HSPG2
AGRN
COL4A2
LAMA5
LAMB2
0.20%
0.15%
0.10%
0.05%
D14
D18
D25

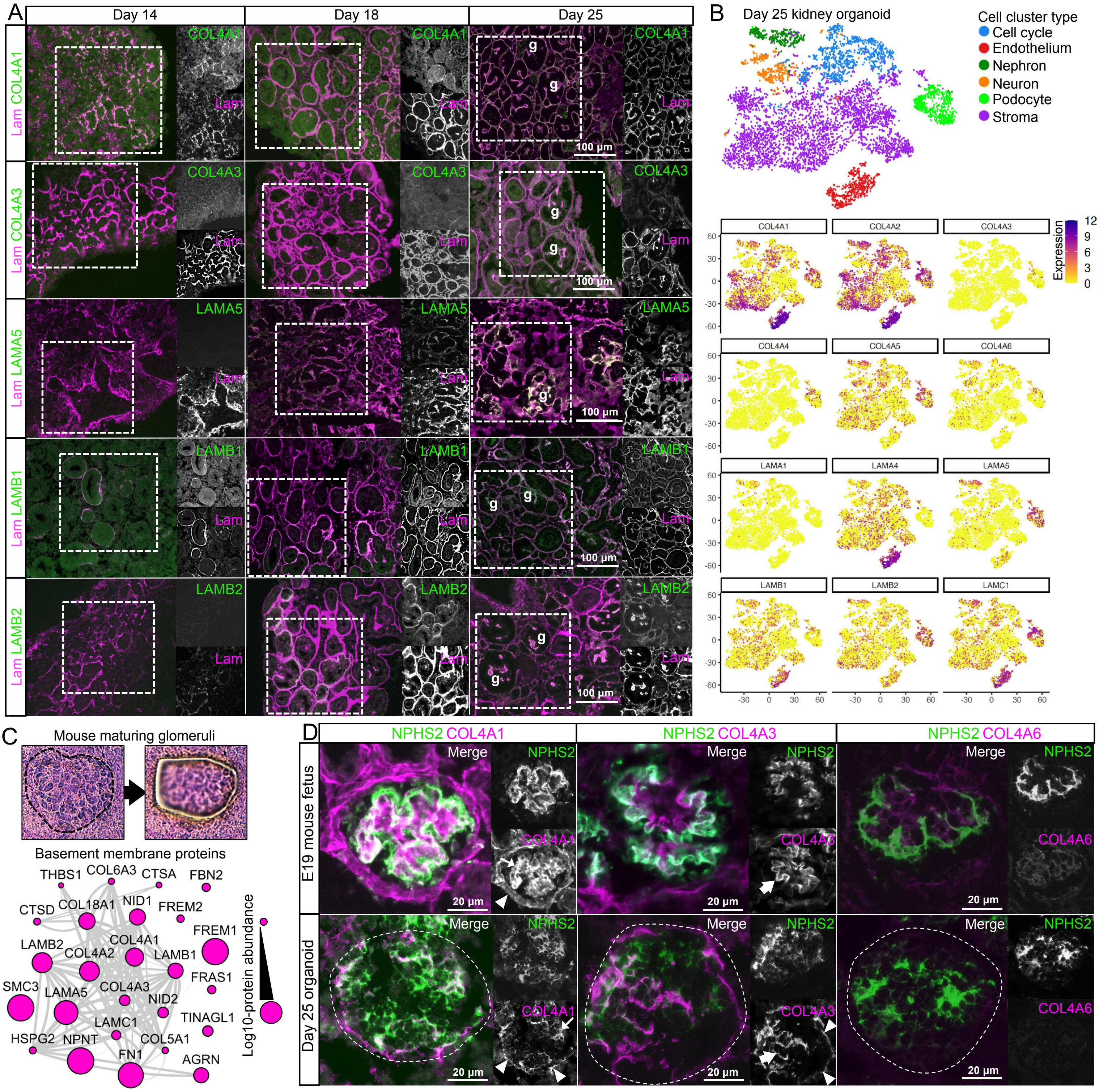
A
Day 14
Day 18
Day 25
Lam COL4A1
Lam COL4A3
Lam LAMA5
Lam LAMB1
Lam LAMB2
COL4A1
COL4A3
LAMA5
LAMB1
LAMB2
Lam
g
100 µm
B
Day 25 kidney organoid
Cell cluster type
Cell cycle
Endothelium
Nephron
Neuron
Podocyte
Stroma
COL4A1
COL4A2
COL4A3
COL4A4
COL4A5
COL4A6
LAMA1
LAMA4
LAMA5
LAMB1
LAMB2
LAMC1
Expression
12
9
6
3
0
60
30
0
-30
-60
C
Mouse maturing glomeruli
Basement membrane proteins
THBS1
COL6A3
CTSA
FBN2
CTSD
COL18A1
NID1
FREM2
FREM1
LAMB2
COL4A1
COL4A2
LAMB1
FRAS1
SMC3
LAMA5
COL4A3
NID2
TINAGL1
LAMC1
HSPG2
NPNT
COL5A1
FN1
AGRN
Log10-protein abundance
D
NPHS2 COL4A1
NPHS2 COL4A3
NPHS2 COL4A6
E19 mouse fetus
Day 25 organoid
Merge
NPHS2
COL4A1
COL4A3
COL4A6
20 µm

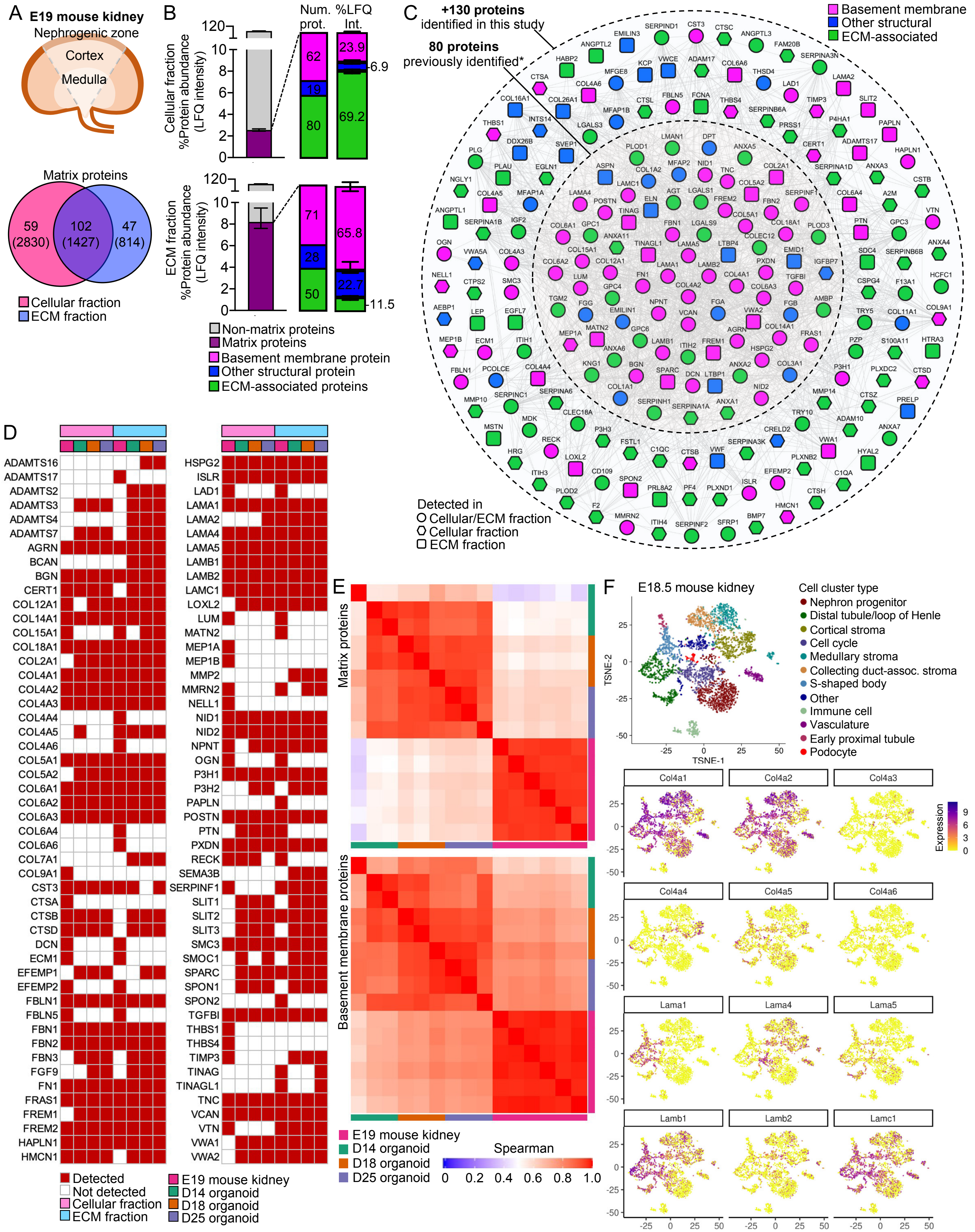

	Cellular fraction				ECM fraction			
	E19 mouse kidney	D14 organoid	D18 organoid	D25 organoid	E19 mouse kidney	D14 organoid	D18 organoid	D25 organoid
ADAMTS16	□	□	□	□	□	□	■	■
ADAMTS17	□	□	□	□	■	□	□	□
ADAMTS2	□	□	□	□	□	■	■	■
ADAMTS3	□	■	■	■	□	■	■	■
ADAMTS4	□	□	□	□	□	■	■	■
ADAMTS7	□	■	■	■	□	■	■	■
AGRN	■	■	■	■	■	■	■	■
BCAN	□	□	□	□	□	■	■	■
BGN	■	■	■	■	■	■	■	■
CERT1	■	■	■	■	□	■	■	■
COL12A1	■	□	■	■	■	■	■	■
COL14A1	■	■	■	■	■	■	■	■
COL15A1	■	□	□	□	■	□	■	■
COL18A1	■	■	■	■	■	■	■	■
COL2A1	□	■	■	■	■	■	■	■
COL4A1	■	■	■	■	■	■	■	■
COL4A2	■	■	■	■	■	■	■	■
COL4A3	■	■	■	■	■	■	■	■
COL4A4	□	□	□	□	■	□	□	□
COL4A5	□	■	□	□	■	■	■	■
COL4A6	□	□	□	□	■	□	□	□
COL5A1	■	■	■	■	■	■	■	■
COL5A2	□	■	■	■	■	■	■	■
COL6A1	■	■	■	■	■	■	■	■
COL6A2	■	■	■	■	■	■	■	■
COL6A3	■	■	■	■	■	■	■	■
COL6A4	□	□	□	□	■	□	□	□
COL6A6	□	□	□	□	■	□	□	□
COL7A1	□	□	□	□	□	■	■	■
COL9A1	■	□	□	□	□	□	□	□
CST3	■	■	■	■	■	■	□	■
CTSA	■	□	□	□	□	□	□	□
CTSB	■	■	■	■	□	■	■	■
CTSD	■	■	■	■	□	■	■	■
DCN	■	□	□	□	■	□	□	□
ECM1	■	□	□	□	■	□	□	□
EFEMP1	□	■	■	■	□	□	■	■
EFEMP2	■	□	□	□	■	□	□	□
FBLN1	■	■	■	■	■	■	■	■
FBLN5	■	□	□	□	■	□	□	□
FBN1	■	■	■	■	■	■	■	■
FBN2	■	■	■	■	■	■	■	■
FBN3	□	■	■	■	□	■	■	■
FGF9	□	□	■	■	□	■	■	■
FN1	■	■	■	■	■	■	■	■
FRAS1	■	■	■	■	■	■	■	■
FREM1	□	■	■	■	■	■	■	■
FREM2	■	■	■	■	■	■	■	■
HAPLN1	■	■	■	■	■	■	■	■
HMCN1	■	■	■	■	□	■	■	■

	Cellular fraction				ECM fraction			
	E19 mouse kidney	D14 organoid	D18 organoid	D25 organoid	E19 mouse kidney	D14 organoid	D18 organoid	D25 organoid
HSPG2	■	■	■	■	■	■	■	■
ISLR	■	■	■	■	■	■	■	■
LAD1	■	□	□	□	■	□	□	□
LAMA1	■	■	■	■	■	■	■	■
LAMA2	□	□	□	■	■	■	■	■
LAMA4	■	■	■	■	■	■	■	■
LAMA5	■	■	■	■	■	■	■	■
LAMB1	■	■	■	■	■	■	■	■
LAMB2	■	■	■	■	■	■	■	■
LAMC1	■	■	■	■	■	■	■	■
LOXL2	□	■	■	■	■	■	■	■
LUM	■	□	□	□	■	□	□	□
MATN2	□	□	□	□	■	□	□	□
MEP1A	■	□	□	□	□	□	□	□
MEP1B	■	□	□	□	□	□	□	□
MMP2	□	□	□	□	□	■	■	■
MMRN2	■	□	□	□	■	□	■	■
NELL1	■	□	□	□	□	□	□	□
NID1	■	■	■	■	■	■	■	■
NID2	■	■	■	■	■	■	■	■
NPNT	■	□	■	■	■	■	■	■
OGN	■	□	□	□	■	□	□	□
P3H1	■	■	■	■	■	■	■	■
P3H2	□	□	■	■	□	■	■	■
PAPLN	□	□	□	□	■	□	□	□
POSTN	■	■	■	■	■	■	■	■
PTN	□	■	■	■	■	□	□	□
PXDN	■	■	■	■	■	■	■	■
RECK	■	■	■	□	■	□	□	□
SEMA3B	□	□	□	□	□	■	■	■
SERPINF1	■	□	□	□	■	■	■	■
SLIT1	□	■	■	■	□	■	■	■
SLIT2	□	■	■	■	■	■	■	■
SLIT3	□	■	■	■	□	■	■	■
SMC3	■	■	■	■	■	■	■	■
SMOC1	□	■	□	■	□	■	■	■
SPARC	□	■	■	■	■	■	■	■
SPON1	□	■	■	■	□	■	■	■
SPON2	□	□	□	□	■	□	□	□
TGFBI	■	■	■	■	■	■	■	■
THBS1	■	□	□	□	□	□	□	□
THBS4	■	□	□	□	□	□	□	□
TIMP3	■	□	□	□	□	■	■	■
TINAG	□	□	□	□	■	□	□	■
TINAGL1	□	□	□	□	■	□	□	■
TNC	■	■	■	■	■	■	■	■
VCAN	■	■	■	■	■	■	■	■
VTN	■	□	□	□	■	■	■	■
VWA1	□	■	■	■	■	■	■	■
VWA2	□	■	■	■	■	■	■	■

■ Detected
□ Not detected

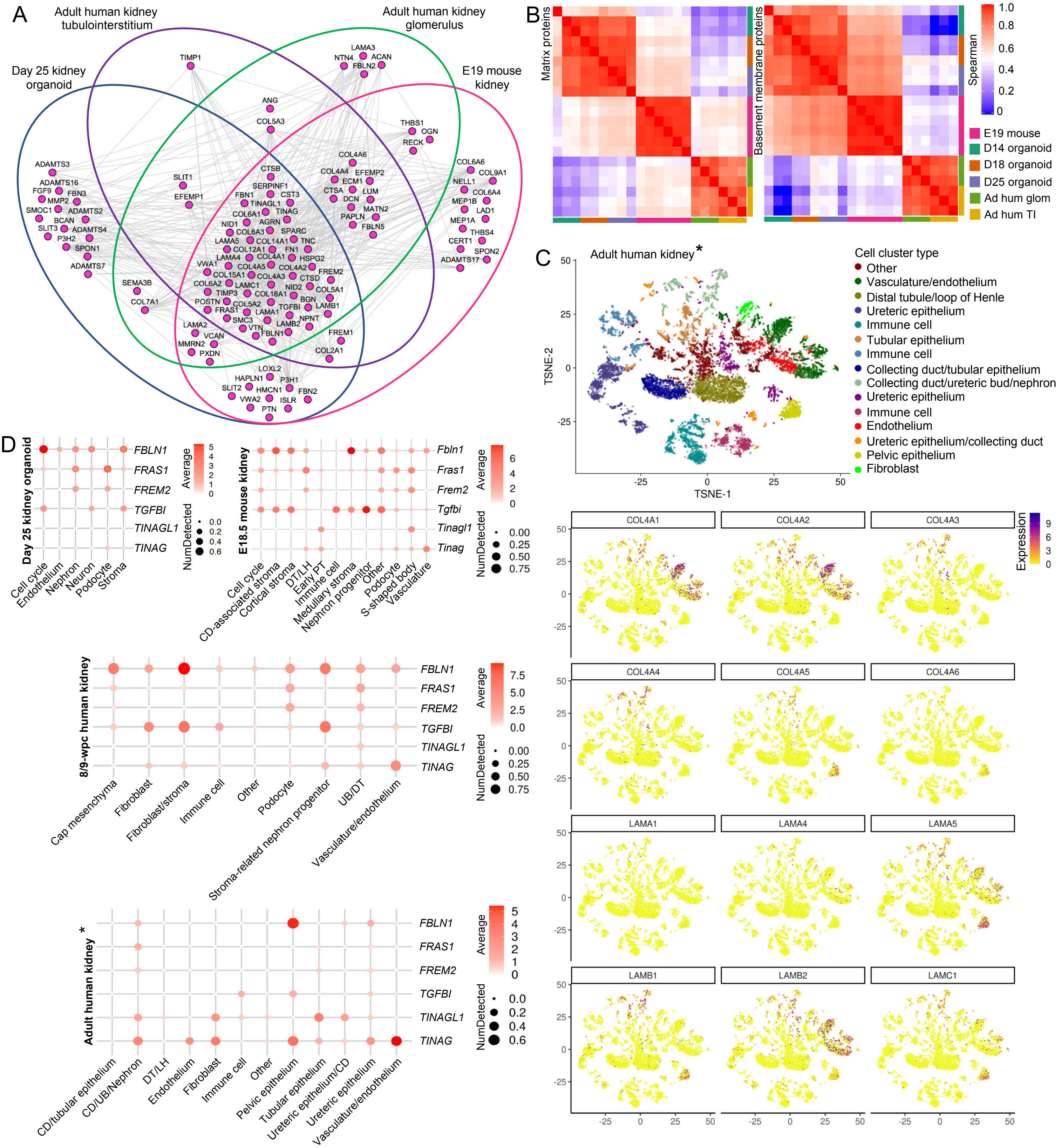
A
Adult human kidney tubulointerstitium
Adult human kidney glomerulus
Day 25 kidney organoid
E19 mouse kidney
TIMP1
LAMA3
NTN4
ACAN
FBLN2
ANG
COL5A3
THBS1
OGN
RECK
ADAMTS3
ADAMTS16
FGF9
FBN3
MMP2
SMOC1
ADAMTS2
BCAN
SLIT3
ADAMTS4
P3H2
SPON1
ADAMTS7
SLIT1
EFEMP1
SEMA3B
COL7A1
COL4A6
COL6A6
COL9A1
NELL1
COL6A4
MEP1B
LAD1
MEP1A
THBS4
CERT1
SPON2
ADAMTS17
CTSB
SERPINF1
FBN1
CST3
TINAGL1
COL6A1
TINAG
COL4A4
EFEMP2
ECM1
CTSA
LUM
DCN
MATN2
PAPLN
FBLN5
NID1
AGRN
COL6A3
SPARC
LAMA5
COL14A1
TNC
COL12A1
FN1
LAMA4
COL4A1
HSPG2
VWA1
COL4A5
COL4A2
FREM2
COL15A1
COL4A3
CTSD
COL6A2
LAMC1
NID2
COL5A1
TIMP3
COL18A1
POSTN
BGN
COL5A2
TGFBI
LAMB1
FRAS1
LAMA1
SMC3
NPNT
VTN
LAMB2
FBLN1
LAMA2
VCAN
FREM1
MMRN2
PXDN
COL2A1
LOXL2
HAPLN1
P3H1
SLIT2
HMCN1
FBN2
VWA2
ISLR
PTN
B
Matrix proteins
Basement membrane proteins
Spearman
1.0
0.8
0.6
0.4
0.2
0
E19 mouse
D14 organoid
D18 organoid
D25 organoid
Ad hum glom
Ad hum TI
C
Adult human kidney*
Cell cluster type
Other
Vasculature/endothelium
Distal tubule/loop of Henle
Ureteric epithelium
Immune cell
Tubular epithelium
Immune cell
Collecting duct/tubular epithelium
Collecting duct/ureteric bud/nephron
Ureteric epithelium
Immune cell
Endothelium
Ureteric epithelium/collecting duct
Pelvic epithelium
Fibroblast
TSNE-2
TSNE-1
50
25
0
-25
-25
0
25
50
COL4A1
COL4A2
COL4A3
COL4A4
COL4A5
COL4A6
LAMA1
LAMA4
LAMA5
LAMB1
LAMB2
LAMC1
Expression
9
6
3
0
D
Day 25 kidney organoid
FBLN1
FRAS1
FREM2
TGFBI
TINAGL1
TINAG
Cell cycle
Endothelium
Nephron
Neuron
Podocyte
Stroma
Average
5
4
3
2
1
0
NumDetected
0.0
0.2
0.4
0.6
E18.5 mouse kidney
Fbln1
Fras1
Frem2
Tgfbi
Tinagl1
Tinag
Cell cycle
CD-associated stroma
Cortical stroma
DT/LH
Early PT
Immune cell
Medullary stroma
Nephron progenitor
Other
Podocyte
S-shaped body
Vasculature
Average
6
4
2
0
NumDetected
0.00
0.25
0.50
0.75
8/9-wpc human kidney
FBLN1
FRAS1
FREM2
TGFBI
TINAGL1
TINAG
Cap mesenchyma
Fibroblast
Fibroblast/stroma
Immune cell
Other
Podocyte
Stroma-related nephron progenitor
UB/DT
Vasculature/endothelium
Average
7.5
5.0
2.5
0.0
NumDetected
0.00
0.25
0.50
0.75
Adult human kidney*
FBLN1
FRAS1
FREM2
TGFBI
TINAGL1
TINAG
CD/tubular epithelium
CD/UB/Nephron
DT/LH
Endothelium
Fibroblast
Immune cell
Other
Pelvic epithelium
Tubular epithelium
Ureteric epithelium/CD
Ureteric epithelium
Vasculature/endothelium
Average
5
4
3
2
1
0
NumDetected
0.0
0.2
0.4
0.6

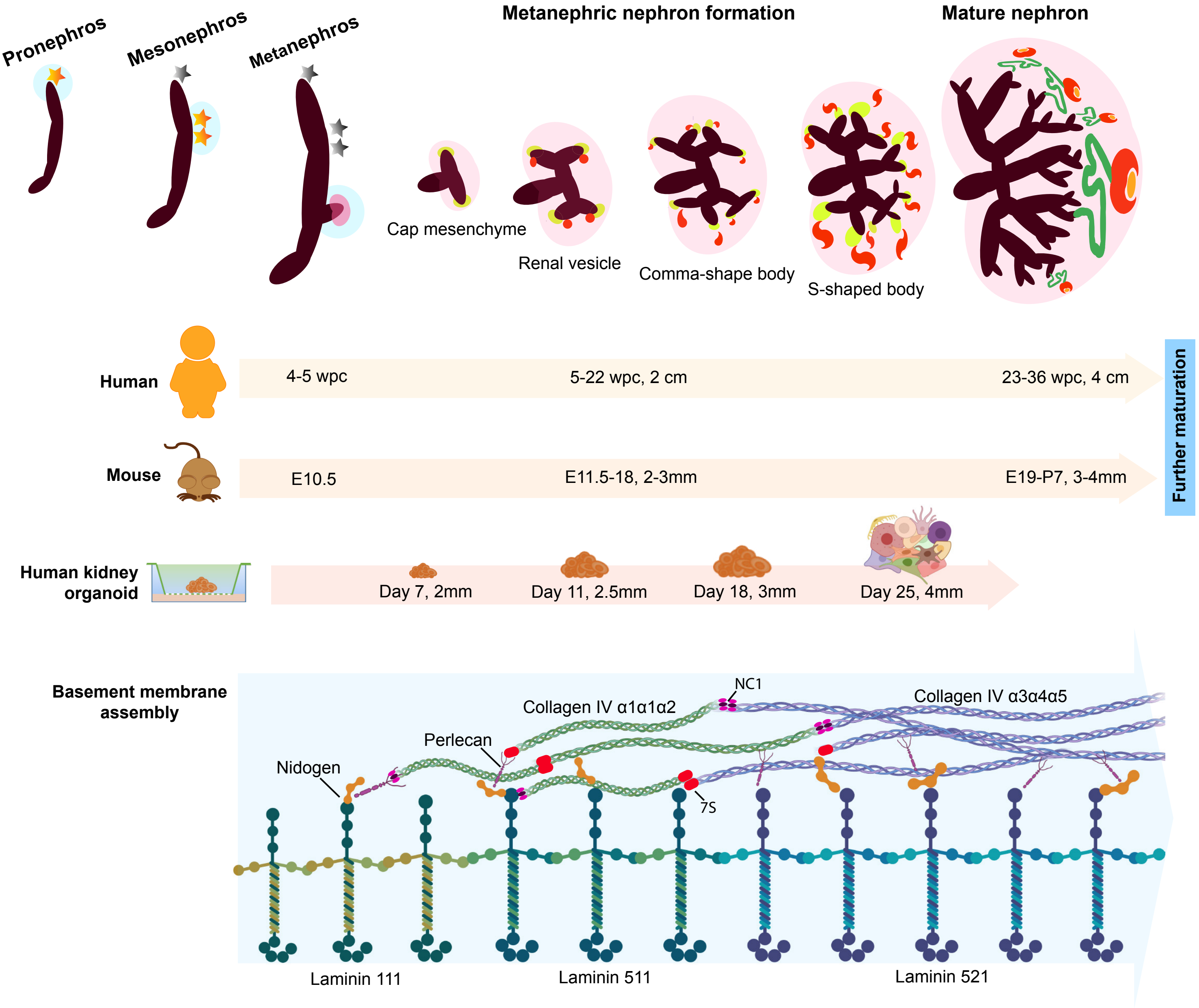
Pronephros
Mesonephros
Metanephros
Metanephric nephron formation
Mature nephron
Cap mesenchyme
Renal vesicle
Comma-shape body
S-shaped body
Human
4-5 wpc
5-22 wpc, 2 cm
23-36 wpc, 4 cm
Mouse
E10.5
E11.5-18, 2-3mm
E19-P7, 3-4mm
Further maturation
Human kidney organoid
Day 7, 2mm
Day 11, 2.5mm
Day 18, 3mm
Day 25, 4mm
Basement membrane assembly
NC1
Collagen IV α1α1α2
Collagen IV α3α4α5
Perlecan
Nidogen
7S
Laminin 111
Laminin 511
Laminin 521

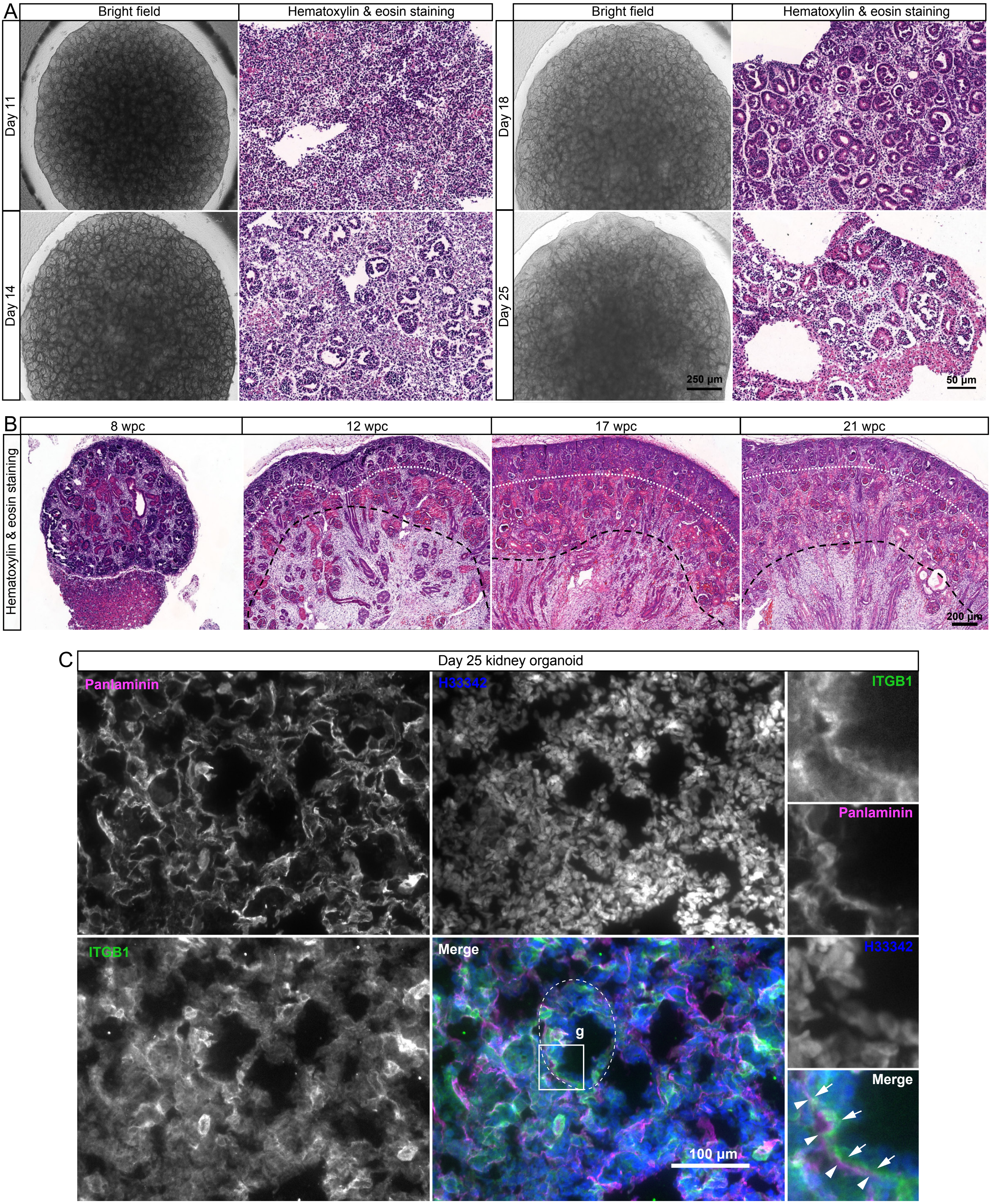

Figure 1-figure supplement 1. Morphological characteristics of wild-type kidney organoids and fetal human kidney. (A) Bright field images (left) and H&E staining (right) of human kidney organoids on day 11, 14, 18 and 25 of differentiation. (B) H&E staining of human fetal kidney at 8 wpc, 12 wpc, 17 wpc, and 21 wpc highlights normal human kidney development. (C) Immunofluorescence for integrin beta-1 (ITGB1) in day 25 kidney organoid (wild-type). Anti-panlaminin or anti-collagen IV antibodies were used to label basement membranes. In the glomerulus (g), note the distribution of ITGB1 adjacent to the basement membrane.

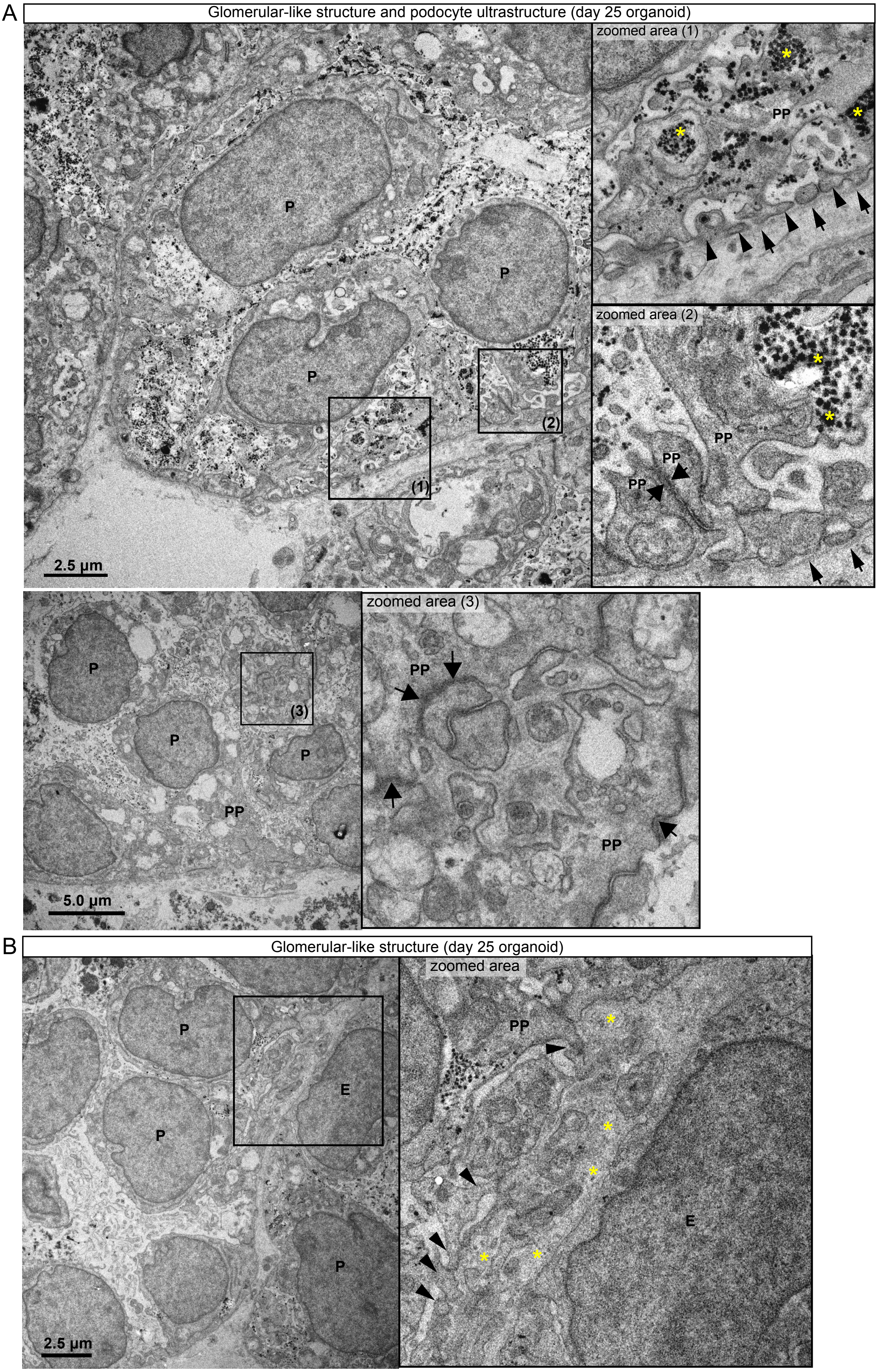

Figure 1-figure supplement 2. Ultrastructure of glomerular-like structures in day 25 human kidney organoids. (A) Transmission electron microscopy of day 25 kidney organoids show advanced differentiation of glomerular structures. In the zoomed areas (1 and 2) note podocytes (P) displaying long branching primary processes (PP) and a layer of intercalated foot processes (thin arrow) lining a distinct basement membrane (thin arrows). Asterisks indicate accumulation of glycogen granules, and large arrowheads tight cell junctions between maturing podocyte processes. In the lower panels, note in the zoomed area (3) a deposition of basement membrane-like matrix between podocyte processes within a glomerular structure. (B) Note the presence of likely endothelial cells (E) and podocytes (P). In the zoomed area, note a layer of podocyte foot processes (arrowheads) and an endothelial cell (E), but deposition of matrix- and BM-like electron-dense material in between (asterisks).

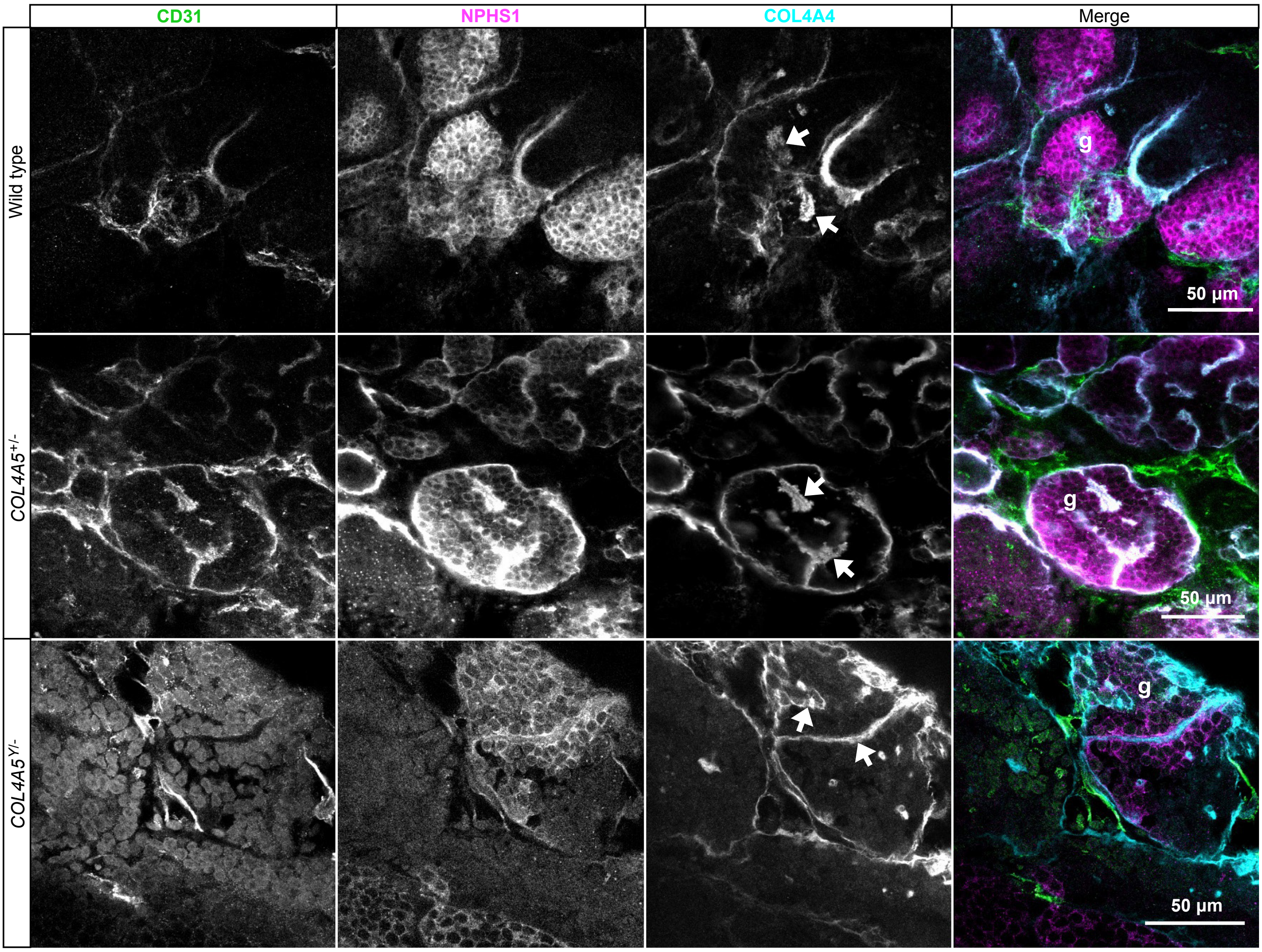

Figure 1-figure supplement 3. Differentiation of wild-type and Alport kidney organoids.
Whole-mount immunofluorescence of wild-type and Alport kidney organoids shows comparable deposition of COL4A4 in BM-like structures (arrows) within NPHS1+/CD31+ glomerular-like structures (g).

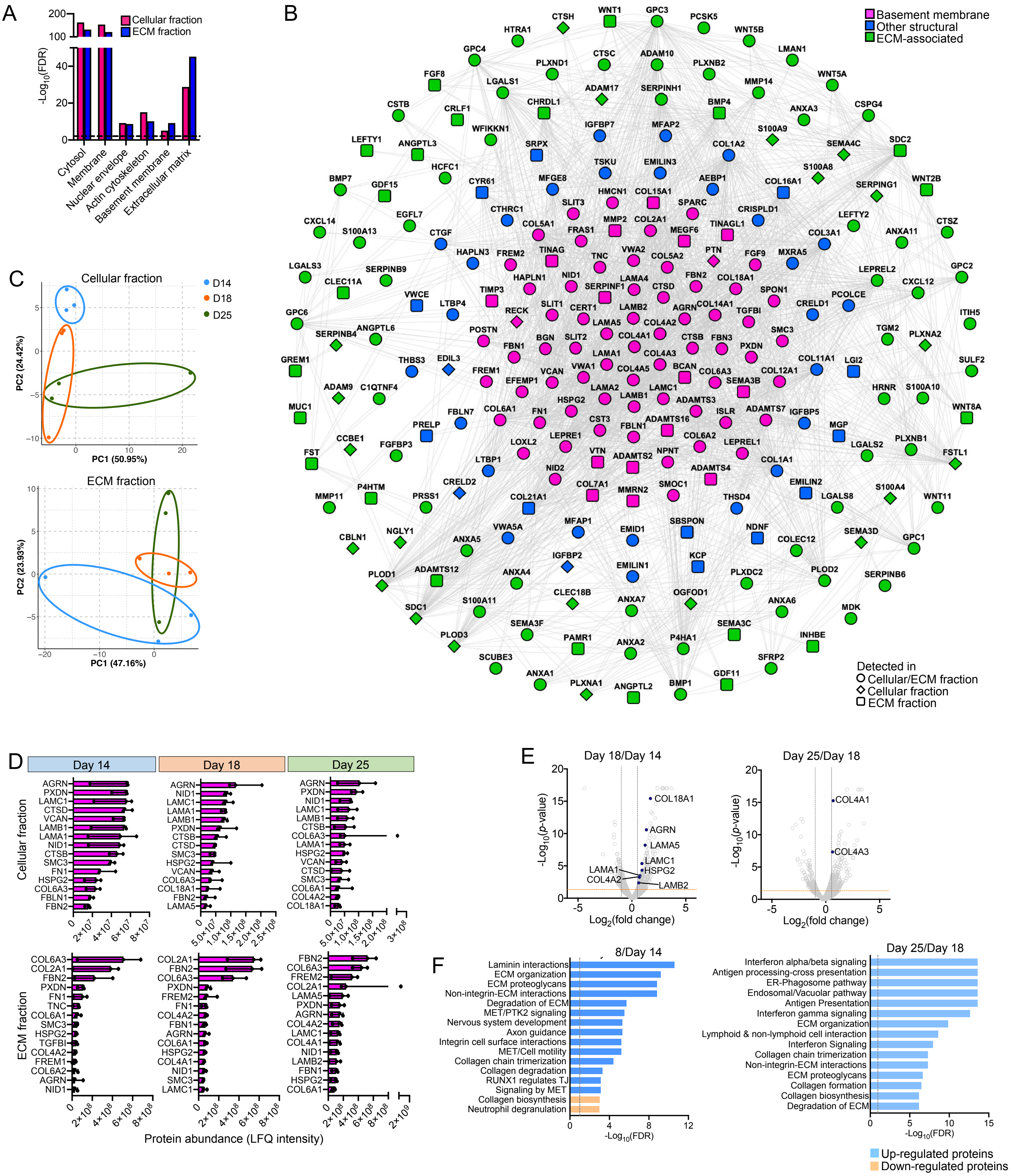

Figure 3-figure supplement 1. Time course proteomic analysis of kidney organoid differentiation. (A) Gene ontology (GO) term enrichment analysis for cellular component annotations associated with proteins detected in the cellular and ECM fractions of kidney organoids by mass spectrometry (MS). GO terms were considered enriched when False Discovery Rate (FDR) < 0.10. (B) Protein interaction network depicts matrisome proteins identified in kidney organoids by MS over the differentiation time course (nodes represent proteins and connecting lines indicate a reported protein-protein interaction). (C) Principal component analysis (PCA) for the matrix proteins identified by MS in the cellular (left plot) and ECM (right plot) fractions of kidney organoids. (D) Top 15 most abundant BM proteins found in kidney organoids by MS. Proteins were ranked according to their normalized abundance levels (LFQ-intensities). Pooled data are shown as median, error bars indicate the 95% confidence interval for the median. (E) Volcano plots show the log2-fold change (x-axis) vs. -log10-p-value (y-axis) for proteins differentially expressed in the cellular fraction of kidney organoids from day 14 to 18, and 18 to 25. Key BM proteins significantly up-regulated (FC>1.5, p-value < 0.05, Two-way ANOVA test, *n*=3) are indicated. (F) Pathway enrichment analysis for proteins differentially expressed during kidney organoid differentiation: bar charts depict log-transformed FDR for the top-most enriched pathways (FDR<0.10). Pathway terms shown were simplified.

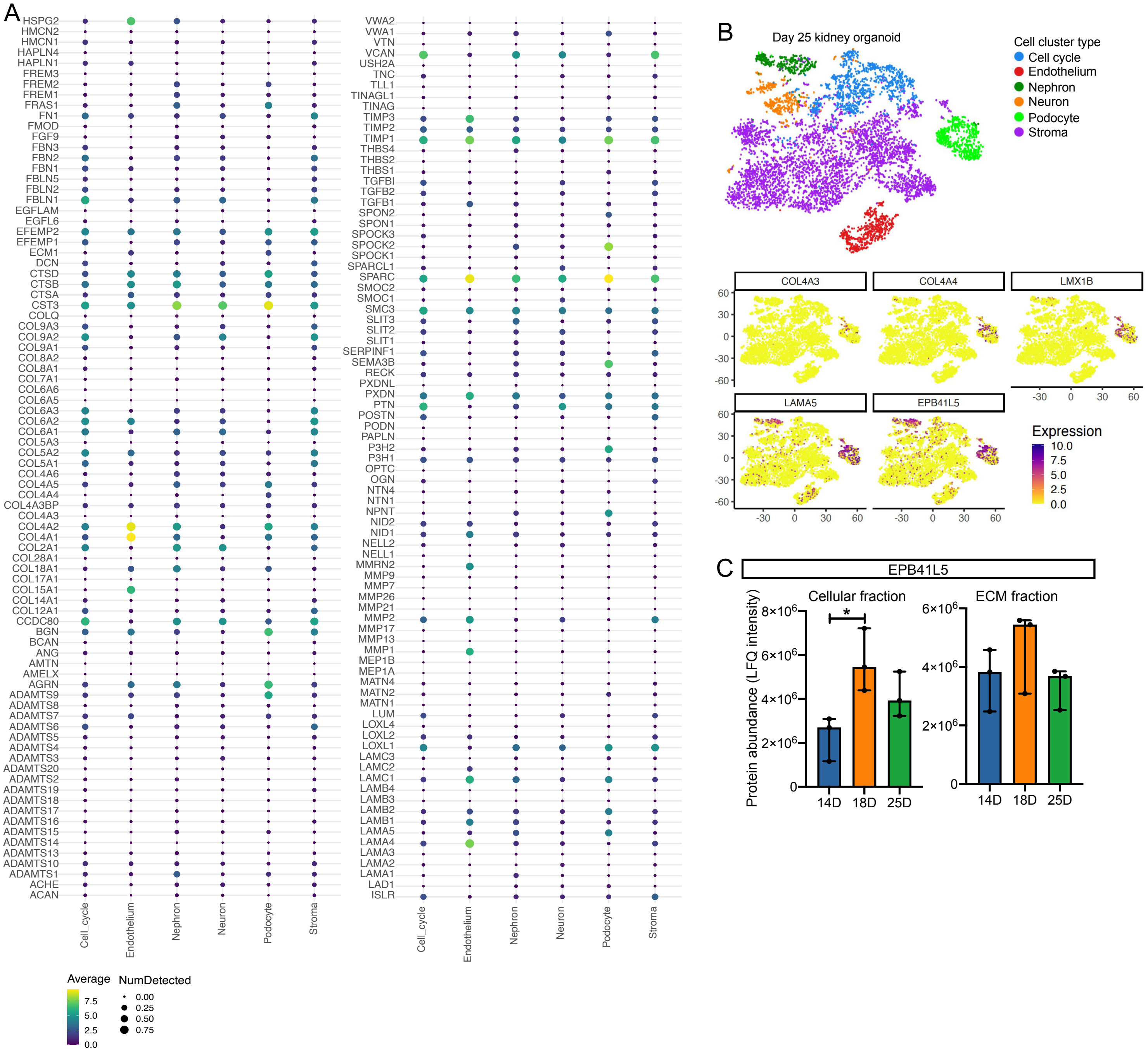

Figure 4-figure supplement 1. Single cell-RNA sequencing data analysis of human kidney organoids.

(A) Dotplot depicting the cell-specific level of expression of 160 BM gene collection in 25 days kidney organoids. (B) tSNE plot indicates gene expression of LIMX1b and EPB41L5 in day 25 kidney organoids. Arrows indicate podocyte clusters. Data shown in (A) and (B) were obtained from a re-analysis of a publicly available scRNA-seq dataset GSE114802 (Combes et al., 2019b). (C) Bar charts show the time-dependent changes in protein abundance of EPB41L5 in kidney organoids (*n*=3 per time point). Pooled data are shown as median, error bars indicate the 95% confidence interval for the median. Two-way ANOVA test: **p*-value <0.05.

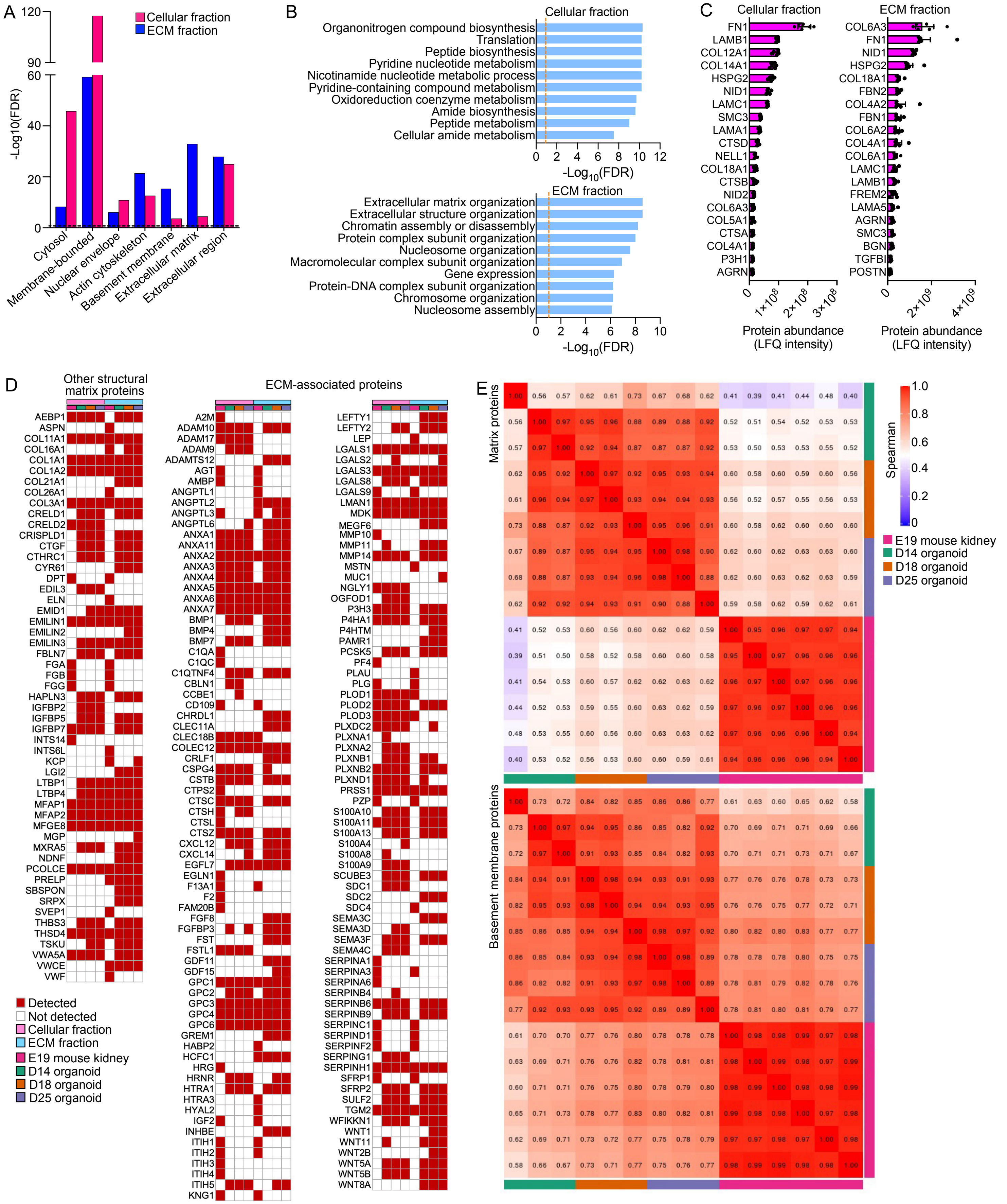

Figure 5-figure supplement 1. Proteomic analysis of E19 mouse fetal kidney and correlational comparison with kidney organoid proteomics. (A) Gene ontology (GO) term enrichment analysis for cellular component annotations associated with proteins detected by MS in the cellular and ECM. (B) GO biological process annotations enriched for top 100 most abundant proteins detected by MS in the cellular and ECM. (C) Top 20 most abundant BM proteins found in the E19 mouse kidney by MS. Proteins were ranked according to their normalized abundance levels (LFQ-intensities). Pooled data are presented as median, error bars indicate the 95% confidence interval for the median. (D) Comparison of other structural matrix and ECM-associated proteins identified in the E19 mouse kidney and kidney organoids over differentiation. (E) Spearman rank correlation plots depicting the r coefficient values for matrix and BM protein abundance (ECM fraction) comparisons between the E19 mouse kidney and kidney organoids.

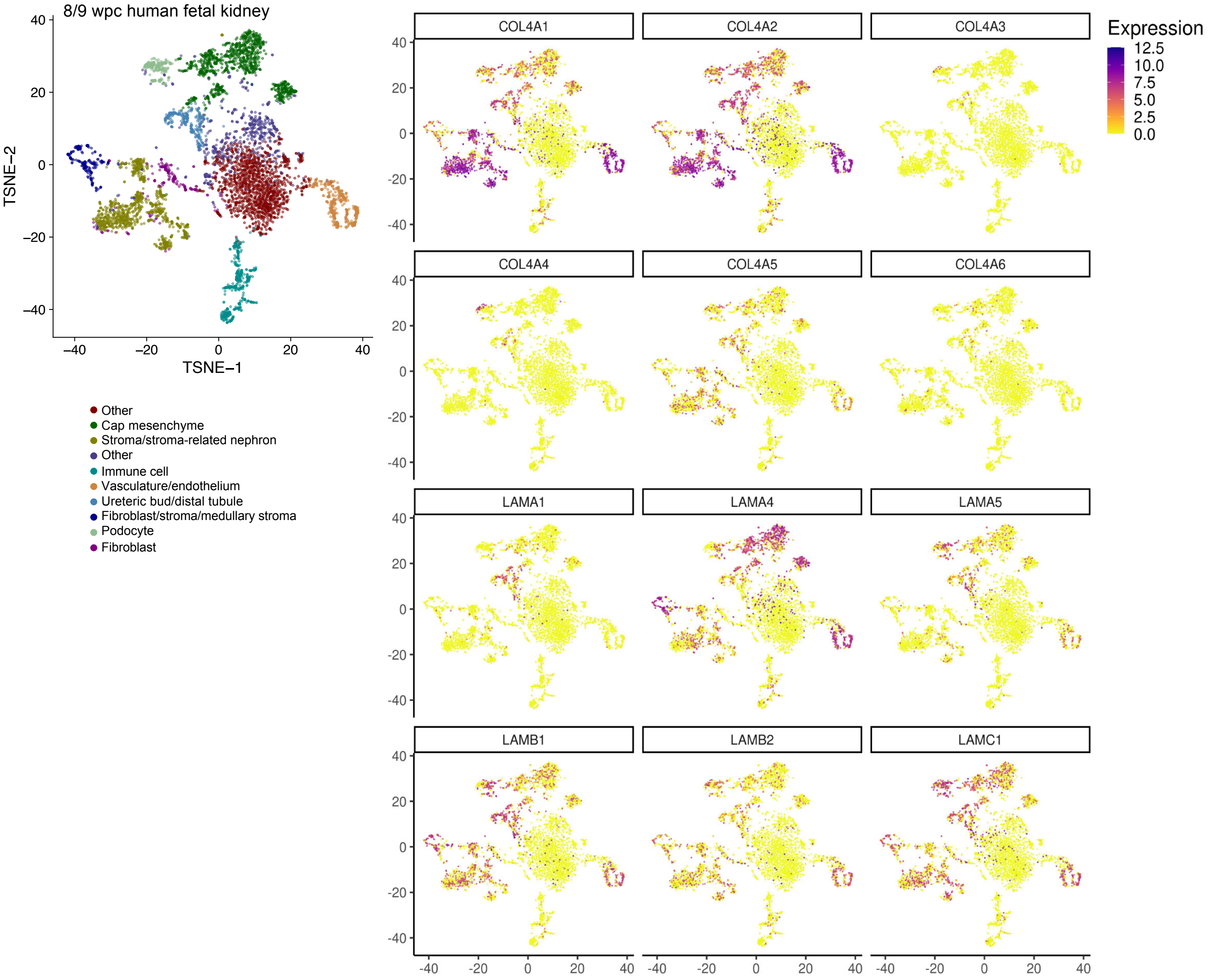

Figure 5-figure supplement 2. Single-cell RNA sequencing analysis of human fetal kidney.
Re-analysis of 8/9-wpc human kidney scRNA-seq datasets (EGAS00001002325, EGAS00001002553; Young et al., 2018) confirms cellular specificity for collagen IV and laminin isoform gene expression. tSNE plots represent the cell type clusters identified, and colour intensity indicates the cell-specific level of expression for the selected BM genes.

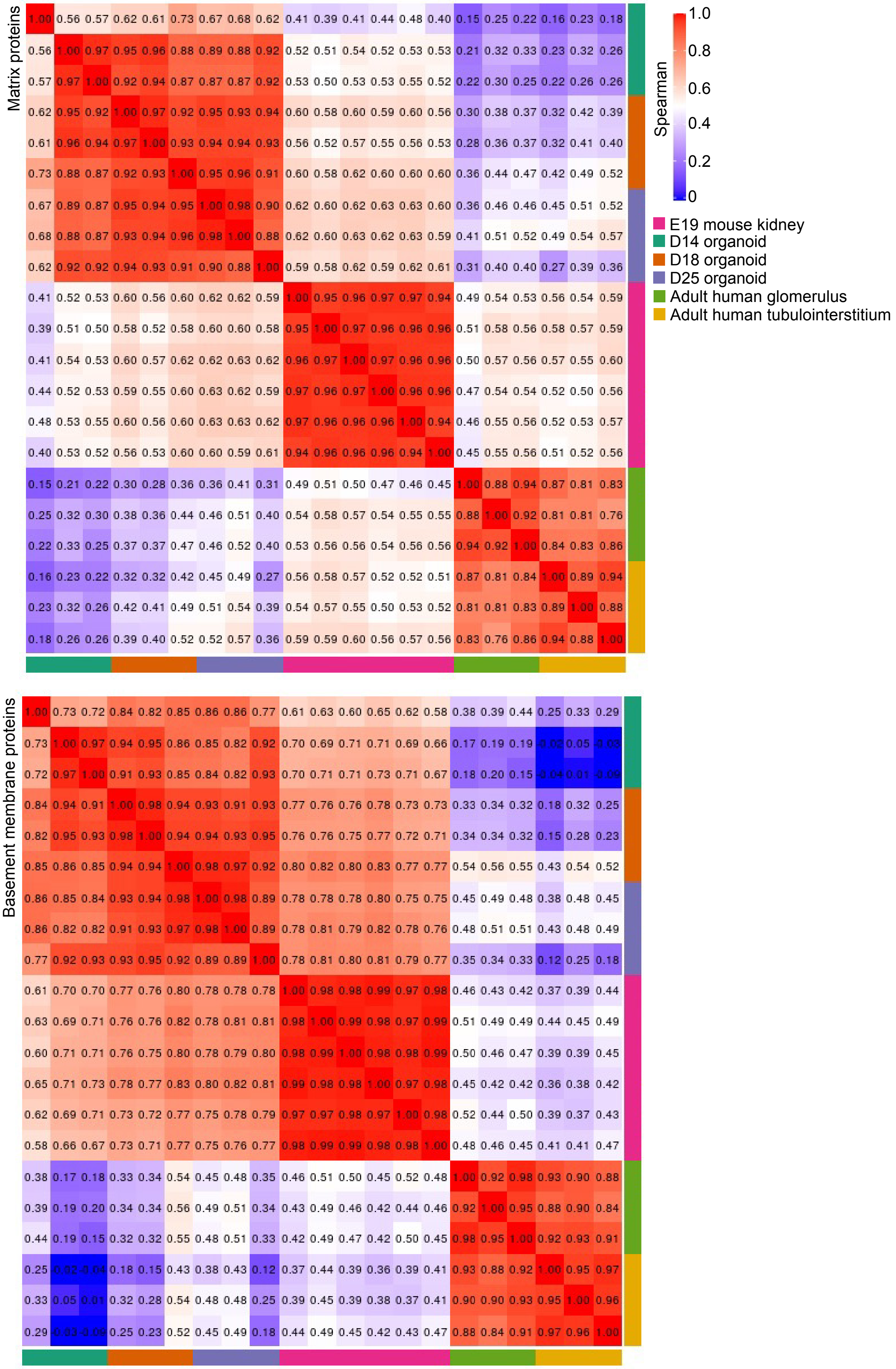

Matrix proteins

1.00	0.56	0.57	0.62	0.61	0.73	0.67	0.68	0.62	0.41	0.39	0.41	0.44	0.48	0.40	0.15	0.25	0.22	0.16	0.23	0.18
0.56	1.00	0.97	0.95	0.96	0.88	0.89	0.88	0.92	0.52	0.51	0.54	0.52	0.53	0.53	0.21	0.32	0.33	0.23	0.32	0.26
0.57	0.97	1.00	0.92	0.94	0.87	0.87	0.87	0.92	0.53	0.50	0.53	0.53	0.55	0.52	0.22	0.30	0.25	0.22	0.26	0.26
0.62	0.95	0.92	1.00	0.97	0.92	0.95	0.93	0.94	0.60	0.58	0.60	0.59	0.60	0.56	0.30	0.38	0.37	0.32	0.42	0.39
0.61	0.96	0.94	0.97	1.00	0.93	0.94	0.94	0.93	0.56	0.52	0.57	0.55	0.56	0.53	0.28	0.36	0.37	0.32	0.41	0.40
0.73	0.88	0.87	0.92	0.93	1.00	0.95	0.96	0.91	0.60	0.58	0.62	0.60	0.60	0.60	0.36	0.44	0.47	0.42	0.49	0.52
0.67	0.89	0.87	0.95	0.94	0.95	1.00	0.98	0.90	0.62	0.60	0.62	0.63	0.63	0.60	0.36	0.46	0.46	0.45	0.51	0.52
0.68	0.88	0.87	0.93	0.94	0.96	0.98	1.00	0.88	0.62	0.60	0.63	0.62	0.63	0.59	0.41	0.51	0.52	0.49	0.54	0.57
0.62	0.92	0.92	0.94	0.93	0.91	0.90	0.88	1.00	0.59	0.58	0.62	0.59	0.62	0.61	0.31	0.40	0.40	0.27	0.39	0.36
0.41	0.52	0.53	0.60	0.56	0.60	0.62	0.62	0.59	1.00	0.95	0.96	0.97	0.97	0.94	0.49	0.54	0.53	0.56	0.54	0.59
0.39	0.51	0.50	0.58	0.52	0.58	0.60	0.60	0.58	0.95	1.00	0.97	0.96	0.96	0.96	0.51	0.58	0.56	0.58	0.57	0.59
0.41	0.54	0.53	0.60	0.57	0.62	0.62	0.63	0.62	0.96	0.97	1.00	0.97	0.96	0.96	0.50	0.57	0.56	0.57	0.55	0.60
0.44	0.52	0.53	0.59	0.55	0.60	0.63	0.62	0.59	0.97	0.96	0.97	1.00	0.96	0.96	0.47	0.54	0.54	0.52	0.50	0.56
0.48	0.53	0.55	0.60	0.56	0.60	0.63	0.63	0.62	0.97	0.96	0.96	0.96	1.00	0.94	0.46	0.55	0.56	0.52	0.53	0.57
0.40	0.53	0.52	0.56	0.53	0.60	0.60	0.59	0.61	0.94	0.96	0.96	0.96	0.94	1.00	0.45	0.55	0.56	0.51	0.52	0.56
0.15	0.21	0.22	0.30	0.28	0.36	0.36	0.41	0.31	0.49	0.51	0.50	0.47	0.46	0.45	1.00	0.88	0.94	0.87	0.81	0.83
0.25	0.32	0.30	0.38	0.36	0.44	0.46	0.51	0.40	0.54	0.58	0.57	0.54	0.55	0.55	0.88	1.00	0.92	0.81	0.81	0.76
0.22	0.33	0.25	0.37	0.37	0.47	0.46	0.52	0.40	0.53	0.56	0.56	0.54	0.56	0.56	0.94	0.92	1.00	0.84	0.83	0.86
0.16	0.23	0.22	0.32	0.32	0.42	0.45	0.49	0.27	0.56	0.58	0.57	0.52	0.52	0.51	0.87	0.81	0.84	1.00	0.89	0.94
0.23	0.32	0.26	0.42	0.41	0.49	0.51	0.54	0.39	0.54	0.57	0.55	0.50	0.53	0.52	0.81	0.81	0.83	0.89	1.00	0.88
0.18	0.26	0.26	0.39	0.40	0.52	0.52	0.57	0.36	0.59	0.59	0.60	0.56	0.57	0.56	0.83	0.76	0.86	0.94	0.88	1.00

Basement membrane proteins

1.00	0.73	0.72	0.84	0.82	0.85	0.86	0.86	0.77	0.61	0.63	0.60	0.65	0.62	0.58	0.38	0.39	0.44	0.25	0.33	0.29
0.73	1.00	0.97	0.94	0.95	0.86	0.85	0.82	0.92	0.70	0.69	0.71	0.71	0.69	0.66	0.17	0.19	0.19	-0.02	0.05	-0.03
0.72	0.97	1.00	0.91	0.93	0.85	0.84	0.82	0.93	0.70	0.71	0.71	0.73	0.71	0.67	0.18	0.20	0.15	-0.04	0.01	-0.09
0.84	0.94	0.91	1.00	0.98	0.94	0.93	0.91	0.93	0.77	0.76	0.76	0.78	0.73	0.73	0.33	0.34	0.32	0.18	0.32	0.25
0.82	0.95	0.93	0.98	1.00	0.94	0.94	0.93	0.95	0.76	0.76	0.75	0.77	0.72	0.71	0.34	0.34	0.32	0.15	0.28	0.23
0.85	0.86	0.85	0.94	0.94	1.00	0.98	0.97	0.92	0.80	0.82	0.80	0.83	0.77	0.77	0.54	0.56	0.55	0.43	0.54	0.52
0.86	0.85	0.84	0.93	0.94	0.98	1.00	0.98	0.89	0.78	0.78	0.78	0.80	0.75	0.75	0.45	0.49	0.48	0.38	0.48	0.45
0.86	0.82	0.82	0.91	0.93	0.97	0.98	1.00	0.89	0.78	0.81	0.79	0.82	0.78	0.76	0.48	0.51	0.51	0.43	0.48	0.49
0.77	0.92	0.93	0.93	0.95	0.92	0.89	0.89	1.00	0.78	0.81	0.80	0.81	0.79	0.77	0.35	0.34	0.33	0.12	0.25	0.18
0.61	0.70	0.70	0.77	0.76	0.80	0.78	0.78	0.78	1.00	0.98	0.98	0.99	0.97	0.98	0.46	0.43	0.42	0.37	0.39	0.44
0.63	0.69	0.71	0.76	0.76	0.82	0.78	0.81	0.81	0.98	1.00	0.99	0.98	0.97	0.99	0.51	0.49	0.49	0.44	0.45	0.49
0.60	0.71	0.71	0.76	0.75	0.80	0.78	0.79	0.80	0.98	0.99	1.00	0.98	0.98	0.99	0.50	0.46	0.47	0.39	0.39	0.45
0.65	0.71	0.73	0.78	0.77	0.83	0.80	0.82	0.81	0.99	0.98	0.98	1.00	0.97	0.98	0.45	0.42	0.42	0.36	0.38	0.42
0.62	0.69	0.71	0.73	0.72	0.77	0.75	0.78	0.79	0.97	0.97	0.98	0.97	1.00	0.98	0.52	0.44	0.50	0.39	0.37	0.43
0.58	0.66	0.67	0.73	0.71	0.77	0.75	0.76	0.77	0.98	0.99	0.99	0.98	0.98	1.00	0.48	0.46	0.45	0.41	0.41	0.47
0.38	0.17	0.18	0.33	0.34	0.54	0.45	0.48	0.35	0.46	0.51	0.50	0.45	0.52	0.48	1.00	0.92	0.98	0.93	0.90	0.88
0.39	0.19	0.20	0.34	0.34	0.56	0.49	0.51	0.34	0.43	0.49	0.46	0.42	0.44	0.46	0.92	1.00	0.95	0.88	0.90	0.84
0.44	0.19	0.15	0.32	0.32	0.55	0.48	0.51	0.33	0.42	0.49	0.47	0.42	0.50	0.45	0.98	0.95	1.00	0.92	0.93	0.91
0.25	-0.02	-0.04	0.18	0.15	0.43	0.38	0.43	0.12	0.37	0.44	0.39	0.36	0.39	0.41	0.93	0.88	0.92	1.00	0.95	0.97
0.33	0.05	0.01	0.32	0.28	0.54	0.48	0.48	0.25	0.39	0.45	0.39	0.38	0.37	0.41	0.90	0.90	0.93	0.95	1.00	0.96
0.29	-0.03	-0.09	0.25	0.23	0.52	0.45	0.49	0.18	0.44	0.49	0.45	0.42	0.43	0.47	0.88	0.84	0.91	0.97	0.96	1.00

Figure 6-figure supplement 1. Integrated correlational analysis of organoid and *in vivo* kidney datasets. Spearman rank correlation plots depicting the r coefficient values for matrix and BM protein abundance (ECM fraction) between E19 mouse kidney, kidney organoids and adult human kidney proteomic datasets.